Journal of Geophysical Research: Solid Earth

RESEARCH ARTICLE

Coseismic Throw Variation Across Along-Strike Bends on Active Normal Faults: Implications for Displacement Versus Length Scaling of Earthquake Ruptures

Francesco Iezzi[1] [ID], **Zoë Mildon[2,3]** [ID], **Joanna Faure Walker[2]** [ID], **Gerald Roberts[1]** [ID], **Huw Goodall[4]** [ID], **Maxwell Wilkinson[5]** [ID], **and Jennifer Robertson[1]** [ID]

[1]Department of Earth and Planetary Sciences, University of London, London, UK, [2]Institute for Risk and Disaster Reduction, University College London, London, UK, [3]Centre for Research in Earth Sciences, School of Geography, Earth, and Environmental Sciences, University of Plymouth, Plymouth, UK, [4]School of Earth and Environment, University of Leeds, Leeds, UK, [5]Geospatial Research Ltd., Department of Earth Sciences, Science Labs, University of Durham, Durham, UK

Abstract Fault bends, and associated changes in fault dip, play a key role in explaining the scatter in maximum offset versus surface rupture length fault scaling relationships. Detailed field measurements of the fault geometry and magnitude of slip in the 2016–2017 Central Italy earthquake sequence, alongside three examples from large historical normal-faulting earthquakes in different tectonic settings, provide multiple examples in which coseismic throw increases across bends in fault strike where dip also increases beyond what is necessary to accommodate a uniform slip vector. Coseismic surface ruptures produced by two mainshocks of the 2016–2017 Central Italy earthquake sequence (24 August 2016 M_w 6.0 and 30 October 2016 M_w 6.5) cross a ~0.83-km amplitude along-strike bend, and the coseismic throws for both earthquakes increase by a factor of 2–3, where the strike of the fault changes by ~28° and the dip increases by 20–25°. We present similar examples from historical normal faulting earthquakes (1887, Sonora earthquake, M_w 7.5; 1981, Corinth earthquakes, M_w 6.7–6.4; and 1983, Borah Peak earthquake, M_w 7.3). We demonstrate that it is possible to estimate the expected change in throw across a bend by applying equations that relate strike, dip, and slip vector to horizontal strain conservation along a nonplanar fault for a single earthquake rupture. The calculated slip enhancement in bends can explain much of the scatter in maximum displacement (*Dmax*) versus surface rupture length scaling relationships. If fault bends are unrecognized, they can introduce variation in *Dmax* that may lead to erroneous inferences of stress drop variability for earthquakes, and exaggerate maximum earthquake magnitudes derived from vertical offsets in paleoseismic data sets.

1. Introduction

Displacement versus length scaling relationships derived from earthquake ruptures are commonly used to infer magnitudes from paleoseismic data and measurements of active fault length and also to calculate stress drops during earthquakes (e.g., Cinti et al., 2011; Dolan et al., 1997; Galadini & Galli, 2000, 2003; Galli et al., 2017; Galli & Peronace, 2014; Manighetti et al., 2007; Pantosti et al., 1996; Villamor & Berryman, 2001). These displacement versus length scaling relationships (e.g., Leonard, 2010; Manighetti et al., 2007; Stirling et al., 2002; Wells & Coppersmith, 1994; Wesnousky, 2008) are widely utilized, yet they are formulated upon data which contains significant scatter in coseismic maximum displacement (*Dmax*) for a given fault length (Figure 1). In this paper we study this scatter and point out that (1) normal faulting earthquake ruptures commonly occur on faults with along-strike bends; (2) these bends appear to be characterized by relatively steep fault dips, as suggested by the five large normal faulting earthquakes studied in this paper; and (3) dip increases within the bends will necessitate an increase in the magnitude of the coseismic slip vector because the coseismic throw and displacement must increase if the coseismic strain is maintained along strike. Our main conclusion is that the increase in the magnitude of the coseismic slip vector, if not recognized, can produce scatter in *Dmax* values for a given fault length, overestimating the value calculated from scaling relationships, and we discuss the implications of this finding.

A key point we make is that bends in fault strike appear to be causal in controlling fault dip (see Figure 2) and the dip is then causal in controlling increases in throw and the magnitude of the slip vector in bends. First, we explain our reasoning concerning how along-strike fault bends form and exert a control on fault dip
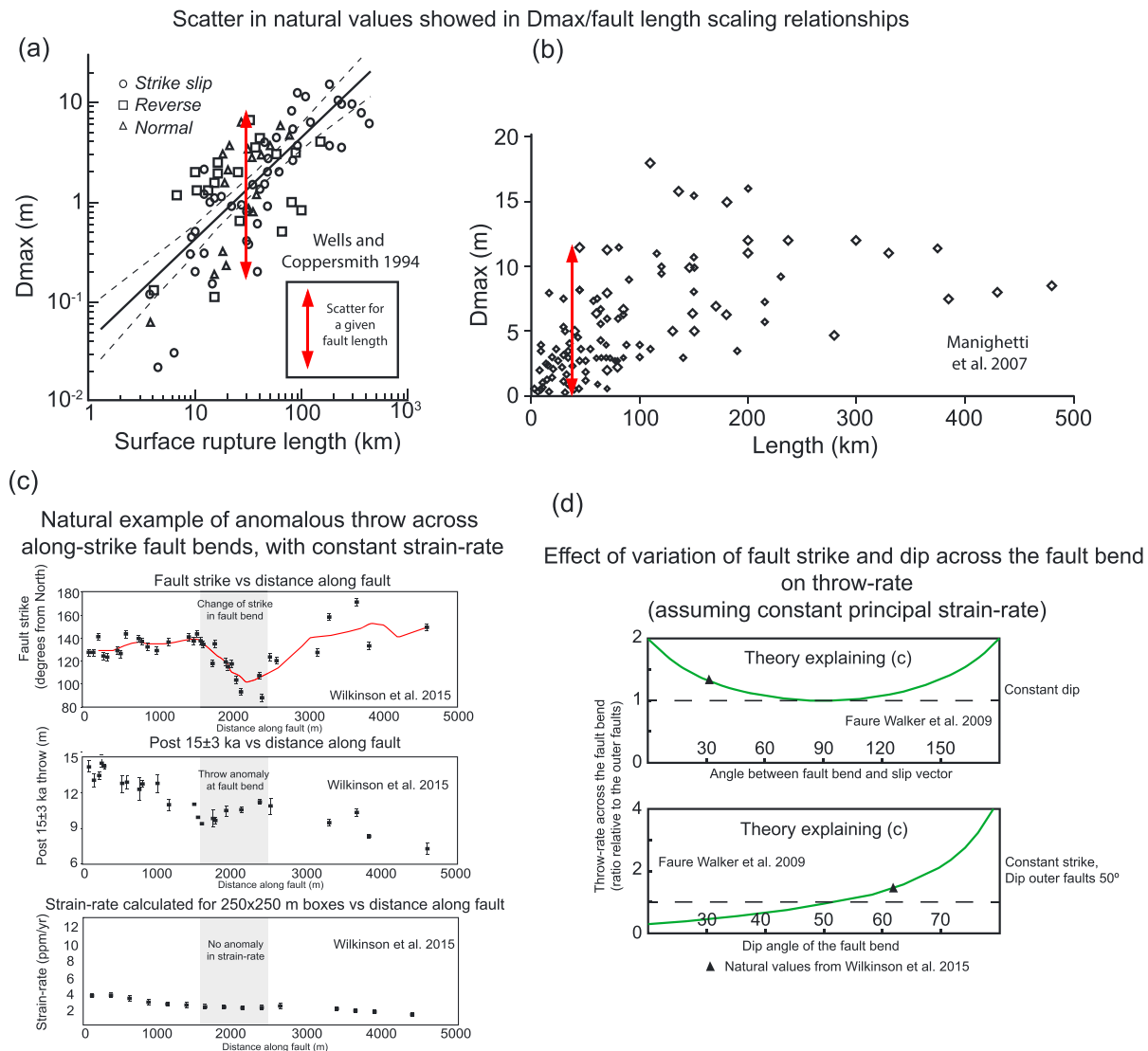
**Figure 1.** Summary of the background literature. (a) Maximum displacement versus fault length scaling relationship from Wells and Coppersmith (1994), Figure 12a. (b) Maximum displacement versus fault length scaling relationship from Manighetti et al. (2007), Figure 3a. Red arrows show scatter of *Dmax* for 30-km fault length in both plots. (c) Relationships between fault strike and post 15 ± 3 ka throw for the Campo Felice fault, central Apennines, Italy (from Wilkinson et al., 2015). The distance 0 km represents the center of the fault, with values increasing moving toward the tip of the fault. Graphs show that instead of having a regular decrease of throw moving toward the tip of the fault, the throw increases within an along-strike fault bend, which is located within 1,500 and 2,500 m. This variation of throw across the fault bend is not accompanied by anomalies in the strain rate distribution along the fault, which decreases regularly toward the tip. (d) Graphs showing relationships between the throw rate and fault strike and dip across a fault bend, with constant strain rate (adapted from Figure 7c and Figure 8c of Faure Walker et al., 2009). Green lines show the variability of the throw rate of the fault caused by the variation of the angle between the fault strike and the slip vector and by the variation of the fault dip within the fault bend. Black triangles are values obtained from Wilkinson et al., 2015, showed in (c).

(Figure 2). Second we explain how dip changes in along-strike bends control the throw and hence magnitude of coseismic slip vectors (Figures 1c and 1d).

First, in terms of how along-strike fault bends form and exert a control on fault dip, we point out that faults grow and link through time (e.g., Mansfield & Cartwright, 2001; Figure 2). What is clear from analogue models for the growth of normal faults (Mansfield & Cartwright, 2001) and fault growth histories in nature described by stratigraphic evolution underpinned by 3-D seismic reflection and age control from well data (e.g., McLeod et al., 2000) is that (1) initially separate faults grow by tip propagation, with en echelon map geometries common; (2) new faults begin to grow in the relay zones between en echelon fault tips as incipient breach faults (see McLeod et al., 2000 for real examples, their Figures 9 and 15, and Mansfield & Cartwright, 2001 for examples in analogue experiments, their Figure 11); (3) the dips of the new breach faults develop to accommodate
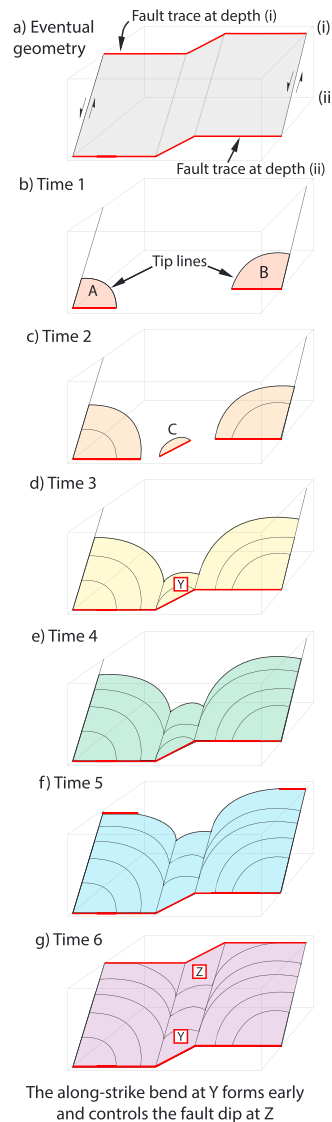
Figure 2. Diagram showing the 3-D evolution of an along-strike fault bend through fault propagation, linkage, and coalescence. This model is adapted from McLeod et al. (2000) and Mansfield and Cartwright (2001). The fault surface at point Z forms after the bend forms at point Y. The dip at point Z for the five earthquakes described in this paper is steeper than for the fault surfaces outside the bend, suggesting this may be typical for such locations. (a) 3-D diagram of the eventual geometry of an along-strike fault bend that developed from two initial en echelon normal faults at depth, which grew through along strike and updip propagation, eventually coalescing into one linked fault surface through time. (b) Time 1: The pink color indicates the fault surface that has formed at this time, with the upper tip line indicated. The faults are still separate faults, A and B. The traces of the faults on the lower surface of the box are shown with a thick red line. (c) Time 2: The orange color indicates the fault surface has grown. The faults are still separate faults. However, a new fault C begins to grow to take up the strain between the faults, working to link the two separate en echelon faults. Fault C is an example of a breach fault (e.g., Faure Walker et al., 2009). All natural examples of earthquake ruptures in this paper show steeper dips in this location compared to the initial en echelon outer faults, so steep dips may well typify such breach faults. We are unaware of examples with shallower dips. (d) Time 3: The yellow color indicates the fault surface has grown and now linked to form the fault surface at point Y. An along-strike bend has formed at depth and is propagating updip. (e) Time 4: The green color indicates further growth and upward propagation. The newly linked fault may also propagate downdip, but this is not shown in this diagram. (f) Time 5: The blue color indicates further growth. The fault begins to intersect the top surface of the box, indicated by thick red lines. Like the bottom surface at time 1, the top surface at time 5 is deformed by two en echelon faults. (g) Time 6: The purple color indicates the final linked fault. The fault bend has fully propagated to the upper surface of the box. The fault surface at point Z forms at time 6. The dip at point Z is steep where it links the two en echelon faults, consistent with observations of the five earthquakes described in this paper. The dip at point Z formed after the along-strike fault bend formed (time 3), and in the five earthquake examples in this paper the dip at point Z is steeper than for the outer faults; this time sequence shows the developing along-strike fault bend is causal in forming the steep dip at Y and Z.

the strain in the relay zone and the regional kinematics (Roberts, 2007; we show below that all the examples presented in this paper have steeper fault dips in the bend); (4) faults then link across the relay zones through tip propagation, followed by coalescence and linkage of breach faults and the initial en echelon faults; and (5) the newly linked fault propagates up and down dip to increase the fault surface area through progressive deformation. The key point is that the dip value for the breach fault, which eventually becomes the fault bend, forms after the formation of the initial en echelon faults and, in updip and downdip locations, after the formation of a throughgoing fault within a bend (see time 6 in Figure 2). In other words, the change in strike across the incipient bend sets up the situation that controls the dip of the eventual fault within the structural bend. The 5 earthquakes described in this paper suggest that relatively steep dips typify such locations (see below). The formation of a steeply dipping breach fault necessitates an increase in throw across the bend if the strain is to be conserved along strike (Faure Walker et al., 2009). Thus, bends in fault strike appear to be causal in controlling steeper fault dips which result in local increases in throw and the magnitude of the slip vector in along-strike fault bends. In summary, along-strike bends are likely to be places where the dip varies and hence the throw varies.

Second, Faure Walker et al. (2009, 2010) show that the vertical offset (throw) across a given location on an active normal fault is controlled by the regional strain the fault must accommodate and the local nonplanar fault geometry. In response to the change in obliquity of the slip across an along-strike fault bend, the throw rate and fault dip must vary locally if the long-term horizontal strain rate across the fault is to be maintained (Faure Walker et al., 2009, 2010, 2015). For an example normal fault from the central Apennines, Italy, local variation in fault strike coincides with a local maximum in throw rate, with preservation of the horizontal strain rate, which decreases linearly toward the fault tip (Figure 1d; Wilkinson et al., 2015). The relationship is confirmed by natural examples of long-term throw rates across faults (e.g., 15 ± 3 ka; Faure Walker et al., 2009; Wilkinson et al., 2015), and individual coseismic ruptures with larger coseismic $Dmax$ within fault bends (Mildon et al., 2016; Wilkinson et al., 2015). If $Dmax$ increases in along-strike fault bends, with steep fault dips, compared to straight faults, and this phenomenon is not recognized, we hypothesize that databases such as that in Wells and Coppersmith (1994), and other published scaling relationships, may contain a mixture of ruptures across along-strike bends and those along straight faults and this may cause scatter in $Dmax$ for a given fault length. This could lead to erroneous inferences about stress drop and maximum magnitude.

To improve our understanding of coseismic throw variations associated with along-strike fault bends with steep fault dips, we present measurements and analysis of the surface ruptures to the 24 August 2016 M_w 6.0 and the 30 October 2016 M_w 6.5 earthquakes that both ruptured the southern part of the Mt. Vettore active normal fault in the central Apennines, Italy. We show that the Mt. Vettore fault exhibits a prominent bend in strike with an associated increase in local fault dip, and a relatively high value of total finite throw and coseismic throw in this bend. We measured the coseismic throw, heave, and displacement independently, with heave derived with trigonometry when it was not possible to measure it directly, within the vertical plane containing the slip vector. The orientation of the slip vector was recorded by mud smears on the fault planes that were striated during coseismic slip, and piercing points in ruptured colluvial deposits. We compare the along-strike profiles of coseismic throw for these two earthquakes with the structural relief and the long-term throw profile of the fault, constructed through geological cross sections, to understand how throw in these earthquakes compares with the longer-term throw of the Mt. Vettore fault. We adapt existing quantitative relationships for the conservation of the horizontal extensional strain rate across fault bends (Faure Walker et al., 2009, 2015) so that they are suitable for single ruptures, to explain the large coseismic throw within the along-strike bend on the Mt. Vettore fault and within along-strike bends for three other large magnitude normal faulting earthquakes. We use these observations to discuss the observed scatter in $Dmax$ in displacement versus length scaling data, and the implications of this for calculating stress-drop variability and maximum estimated magnitudes for paleoearthquakes.

2. Geologic Background

The 2016–2017 Central Italy seismic sequence began on the 24 August 2016 with a M_w 6.0 earthquake that killed 302 people (Figure 3). The earthquake ruptured both the north western part of the Laga fault and the south eastern part of the Mt. Vettore fault with reports of surface ruptures confined to the latter (Livio et al., 2016). On 26 October 2016, two earthquakes (M_w 5.4 and 5.9) ruptured the northern part of the Mt. Vettore
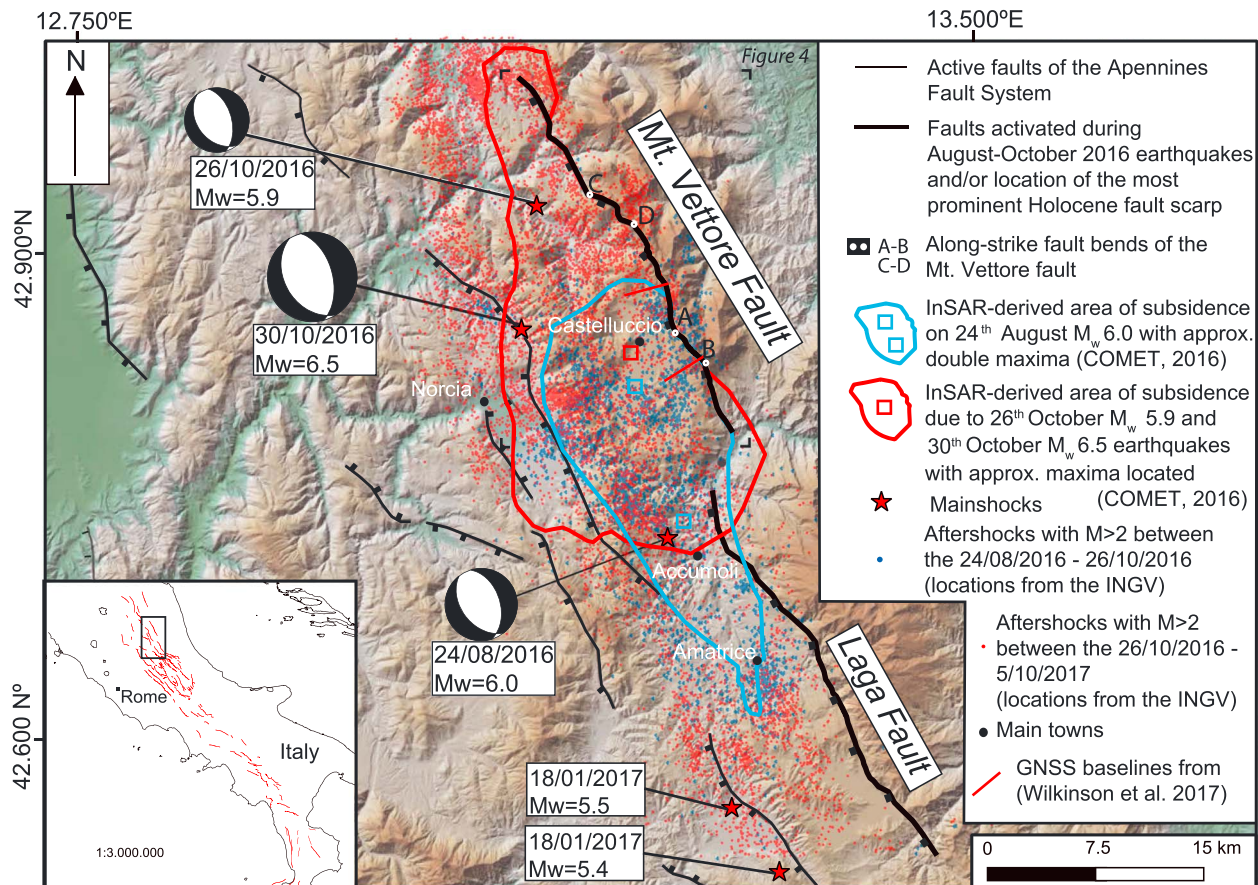
Figure 3. Location map of the 2016 Central Italy seismic sequence. Black lines are active faults, with tick marks on hangingwall; thick black lines are Mt. Vettore and Laga faults, activated during the seismic sequence; the fault traces represent the location of the most prominent Holocene fault scarp. A-B and C-D are the locations of along-strike fault bends of the Mt. Vettore fault. Red stars are the epicentral locations of the mainshocks of the sequence, locations, and M_w from the Istituto Nazionale di Geofisica e Vulcanologia (INGV) (http://cnt.rm.ingv.it); focal mechanisms are from Centroid Moment Tensor (CMT) catalogue (http://rcmt2.bo.ingv.it/Italydataset.html). Blue and red lines are the interferometric synthetic aperture radar(InSAR)-derived area of deformation due to the 24 August M_w 6.0 and to 26 October Mw 5.9 to 30 October M_w 6.5 earthquakes, respectively (COMET, 2016), with the approximate locations of maximum coseismic subsidence indicated. Blue dots are aftershocks with M > 2 recorded between 24 August 2016 and 26 October 2016. Red dots are aftershocks with M > 2 recorded between 26 October 2016 and 5 October 2017 (CMT catalogue).

fault, but it is unclear if they produced surface ruptures. It is unclear because on the 30 October 2016, before field surveys of the 26 October earthquakes, a M_w 6.5 earthquake ruptured the total length of the Mt. Vettore fault, rerupturing locations that slipped in the 24 August 2016 earthquake and perhaps those on the 26 October (see Figures 2, 3, and 4; Calderoni et al., 2017; Cheloni et al., 2017; Chiaraluce et al., 2017; Civico et al., 2018; Falcucci et al., 2018; Ferrario & Livio, 2018; Lavecchia et al., 2016; Mildon et al., 2017; Pavlides et al., 2017; Perouse et al., 2018; Pizzi et al., 2017; Porreca et al., 2018; Scognamiglio et al., 2018; Verdecchia et al., 2018; Villani, Civico, et al., 2018; Villani, Pucci, et al., 2018; Walters et al., 2018). Meter-scale offset across surface ruptures was measured with near-field 1-Hz global navigation satellite system for the 30 October ruptures, revealing that the ruptures formed within 2–4 s and, before peak ground acceleration, supporting the primary tectonic origin of the ruptures (Wilkinson et al., 2017; Figure 3).

These normal faulting earthquakes occurred within the Miocene Apennines fold-and-thrust belt, that in general thrusted Mesozoic and Cenozoic limestones onto Miocene flysch deposits, with NE-SW shortening (Anderson & Jackson, 1987; Doglioni, 1993). Since about 2–3 Ma, SW-NE directed extension started to overprint the thrust belt (Cavinato and De Celles, 1999; Mariucci & Montone, 2016; Roberts et al., 2002), causing the growth of a normal fault system in this new stress field (Cavinato et al., 2002; Patacca et al., 1990; Pizzi and Galadini, 2009; Pizzi and Scisciani, 2000). The normal faults strike ~NW-SE, with lengths of ~20–40 km and total throws less than ~2 km (Pizzi and Scisciani, 2000; Roberts & Michetti, 2004). They form an array of dip-slip faults with the main fault surfaces not physically connected, showing both en echelon and end-
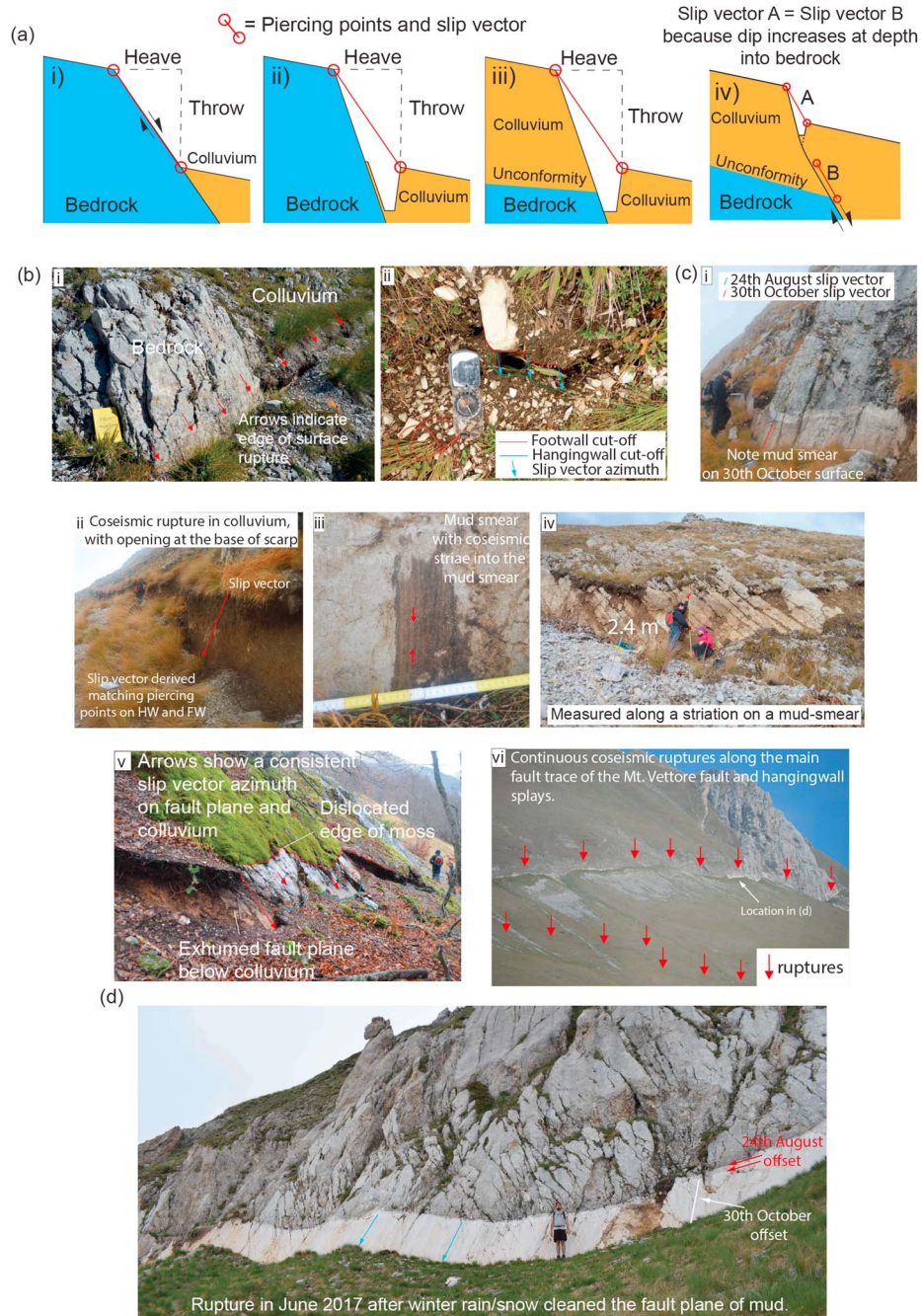
Figure 4. Field observations of the surface ruptures along the Mt. Vettore fault. (a) Cartoons showing the measurements collected on surface ruptures observed in the field. On bedrock fault planes, the slip vector has been measured along the fault plane; the heave was derived using trigonometry. In colluvium, the slip vector has been measured between piercing points on the hangingwall and footwall. (b) Photos of the surface ruptures associated with the 24 August M_w 6.0 earthquake: (bi) coseismic ruptures propagating from bedrock to colluvial deposits without significant variation in slip magnitude; red arrows mark the edge of the rupture on the footwall (notebook for scale, 20 cm tall); (bii) map view of measurements of the slip vector azimuth from reconstruction of the piercing points in colluvial deposits on ground cracks (compass base is about 18 cm long). (c) Photos of the surface ruptures associated with the 30 October M_w 6.5 earthquake: (ci) bedrock fault plane, showing the 24 August rupture (blue line) and the 30 October rupture (red line); (cii) coseismic surface rupture propagating through colluvium, with the formation of a vertical scarp and an opening at its base; in this cases, the slip vector has been measured by matching piercing points on the hangingwall and footwall cutoffs, to obtain the best representation of the slip vector on fault at depth, below the colluvial deposits; (ciii) striations into a mud smear on the fault plane (red arrows indicate the slip vector); (civ) maximum offset observed, displacement 2.4 m measured along a single tool track on a mud smear; (cv) coseismic ruptures on an antithetic fault, with exhumation of the fault plane; red arrows indicate the slip vector azimuth, which is consistent between bedrock fault plane and colluvium (plastic bottle as scale, about 20 cm tall); (cvi) panoramic view of the surface ruptures on the Mt. Vettore fault; the ruptures were continuous along the main fault trace of the Mt. Vettore fault, and hangingwall ruptures also formed. (d) Ruptures in June 2017, after winter rain and snow cleaned the fault plane of mud; fresh stripes of fault plane following the 24 August M_w 6.0 and the 30 October M_w 6.5 are shown, with pale blue arrows indicating the slip vector for the 30 October earthquake.

on arrangements of faults along strike (Roberts & Michetti, 2004). This normal fault system has produced historical seismicity recorded since at least Roman times (Catalogo Parametrico Terremoti Italiani 2015, Rovida et al., 2016), including moderate-to-large earthquakes (up to M_w 6.5–7.0). Fault-specific earthquake recurrence times for surface faulting derived from paleoseismology are in the order of hundreds to thousands of years (Blumetti et al., 1993; Boncio et al., 2004; Cello et al., 1997; Galadini & Galli, 2000).

The Mt. Vettore fault dissects the western slope of the Sibillini Mountain range (Figures 2–4). The fault is about 30 km in length, and its 10^6-year activity has produced an internally draining intramontane basin and lake bed, and a large footwall escarpment (up to 1,000 m of relief). Despite clear geomorphic evidence of Holocene active faulting, there is no record of prior historical earthquakes on the Mt. Vettore fault (see Galadini & Galli, 2000). Paleoseismological analyses of the Mt. Vettore fault suggest a minimum throw rate of 0.11–0.36 mm/year, a recurrence interval that could span at least 4,690 years and a minimum elapsed time of 1,300–1,500 years, but possibly up to 4,155 years since the last paleoearthquake (Galadini & Galli, 2003).

3. Methods

3.1. Measurements

We conducted field mapping of the surface ruptures immediately after the 24 August and 30 October 2016 earthquakes (Figures 4 and 5). The full extent of the 24 August 2016 surface rupture was mapped within a few weeks after the earthquake, and before the occurrence of the 30 October 2016 earthquake (Livio et al., 2016). For the 30 October earthquake, we focused our work on constraining the large coseismic throws around a prominent bend near the southern end of the Mt. Vettore fault (bend A-B, Figure 5), which also ruptured in the earlier 24 August earthquake. We conducted most of the mapping for the 30 October 2016 earthquake from the 2–6 November 2016 but completed a section of the mapping across the A–B bend in June 2017, due to bad weather after the 6 November 2016; the absence of measured postseismic slip larger than ~5 cm, constrained by remeasuring the offset at given sites, allowed us to combine the November and June data sets. The fault trace shows a second prominent along-strike fault bend along its northern half (C-D, Figure 5), which also ruptured during the 30 October M_w 6.5 earthquake (Civico et al., 2018; Villani, Civico, et al., 2018). We were unable to map ruptures across this fault bend with the detail required for this paper in the time available, but those ruptures are described by Civico et al. (2018) and Villani, Civico, et al. (2018).

We measured the strike, dip, slip vector azimuth, plunge of the slip vector, slip vector magnitude, throw, heave, and displacement associated with the ruptures, using steel rulers, compass clinometers, and hand-held global positioning system (Figures 3a, 4–8 and S2 in the supporting information). Measurements were made every 2–10 m along strike and every 10–50 m along strike, following the 24 August 2016 earthquake and the 30 October 2016 earthquake, respectively. We plotted these measurements as a function of distance along a line oriented parallel to the regional strike (163°) of the Mt. Vettore fault (Figures 6 S2, and S3).

Where the ruptures occurred directly on the bedrock fault plane, they revealed a freshly exposed light-colored stripe in the limestone bedrock (Figure 4). In these locations we measured throw and displacement in the vertical plane containing the slip vector, defined by striations on mud smears (Figures 4c and 5), and used trigonometry to derive the heave. The longer-term slip vector orientation was confirmed by kinematic indicators on the fault plane, such as tool marks and frictional wear striae cut into the limestone fault gouge, and measurements of the strike and dip of fault planes.

In places, the ruptures also stepped a few decimeters to meters into the hangingwall of the main bedrock scarp to offset colluvial deposits. To obtain accurate measurements and avoid the effects of disaggregation on colluvial scarps, we used two methods: (1) We measured the slip vector azimuth and the displacement along preserved continuous striae on fault planes cutting through the fine matrix of coarse-grained mixed scree, debris flow, and colluvial deposits, and also the magnitude of the slip vector where possible; (2) where striae were not preserved, we measured the slip vector by matching piercing points on the footwall and hangingwall cutoffs defined by clasts and holes left by clasts in the colluvium (see Figures 4bii and 4cii).

To understand how the offsets produced by these earthquakes compare to offsets that have developed over the long-term history of the Mt. Vettore fault, we compared the along-strike profiles of coseismic throw for the two earthquakes with the long-term throw profile of the fault, constructed from 10 serial geological cross sections across prerift strata, based on the geological map published in Pierantoni et al. (2013) and our own
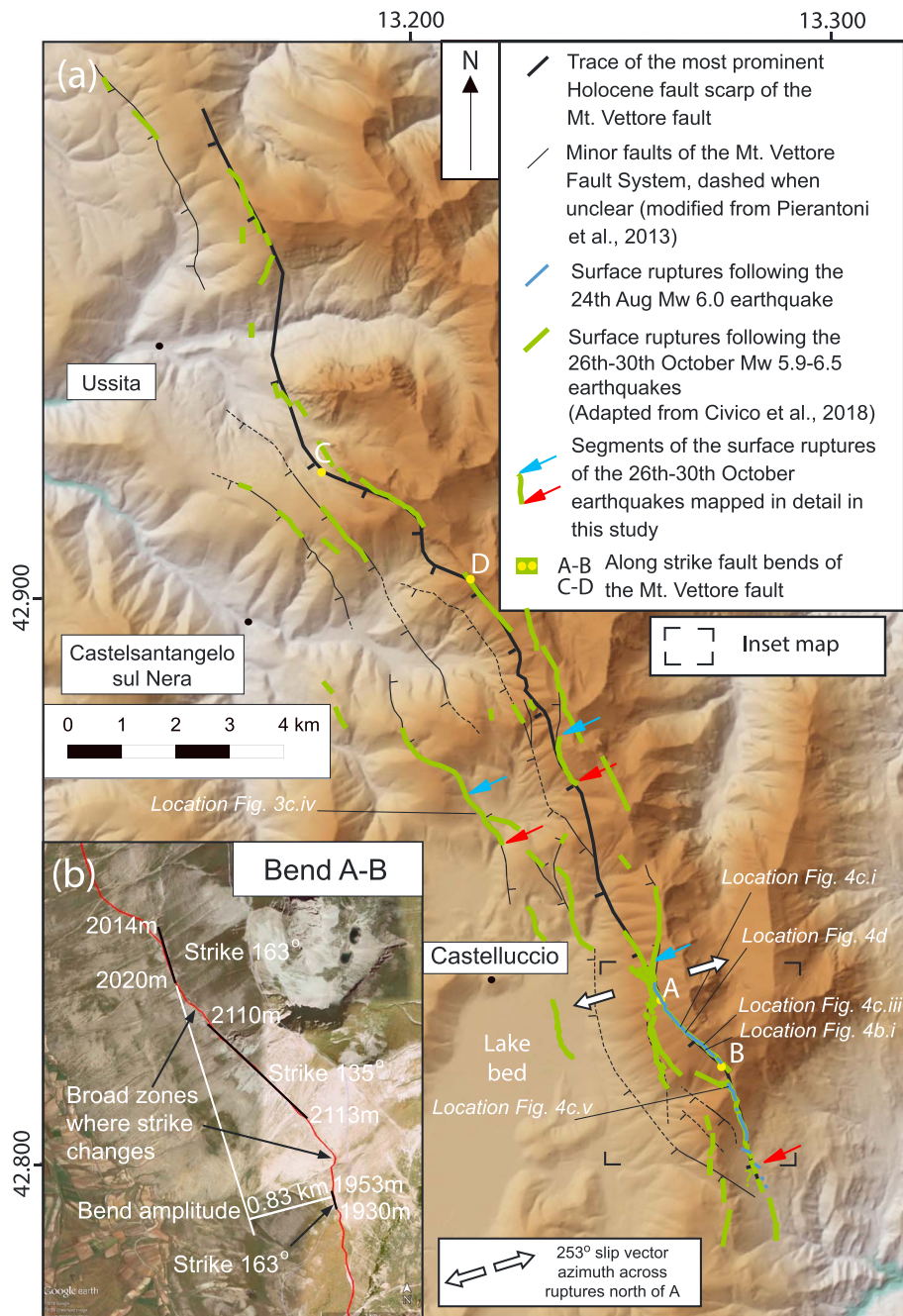
Figure 5. Map of the Mt. Vettore fault. (a) Summary map of the surface ruptures associated with the 2016 Central Italy earthquakes, adapted from Civico et al. (2018) and our own mapping. Fault traces are from the geological map published in Pierantoni et al. (2013). Thick black lines mark the trace of the most prominent Holocene fault scarp of the Mt. Vettore fault. Thin black lines are minor faults of the Mt. Vettore fault system, dashed where not clearly evident at the surface. Pale blue traces are the total coverage of the surface ruptures that occurred after the 24 August earthquake. Green traces are the distribution of the surface ruptures associated with the 30 October earthquake (adapted from Civico et al., 2018). Pale blue and red arrows mark the traces of the surface ruptures following the 30 October earthquake that were mapped and described in detail in this paper. (b) Characterization of the fault bend marked as A-B. Red line is the main fault trace of the Mt. Vettore fault. Black lines are strike lines, which are straight lines joining points at equal elevation on the hangingwall cutoff, providing the best representation of the fault strike for distances that encompass local field measurements (hundreds to thousands meters). The figure shows that within the fault bend the strike changes by about 28°, producing an amplitude of the bend of about 0.83 km. This figure also shows that both earthquakes ruptured across the along-strike fault bend.

field observations (Figure 8; see supporting information S1; Mildon et al., 2017). We also compared these along-strike profiles with (1) the large-scale relief associated with the footwall escarpment on the Mt. Vettore fault obtained using topographic profiles derived from a 10-m resolution digital elevation model (Tarquini et al., 2007, 2012) and (2) the location of Middle Pleistocene-Holocene lake deposits in the hangingwall (from Pierantoni et al., 2013), to ascertain the position and dimensions of areas of maximum subsidence (Figure 8). We have also compared the long-term deformation with the locations of maximum coseismic subsidence determined from preliminary interferometric synthetic aperture radar results (InSAR; Figure 8).

3.2. The Relationship Between Strain, Fault Geometry, and Coseismic Throw

We calculated predicted throws across fault bends by adapting the methodology published in Faure Walker et al. (2009) so that it can be used with individual ruptures, using field measurements as input (Figures 8 and 9). We define an "along-strike bend" as a portion of the fault where the strike is not perpendicular to the regional extension direction. We define outer faults as portions of the fault either side of the bend with strikes that are perpendicular to the regional extension direction. The methodology of Faure Walker et al. (2009), when applied to natural examples, shows that the horizontal strain rate is maintained along strike, even within along-strike fault bends where the dip increases beyond what is necessary to accommodate a uniform slip vector, because variation in fault strike and dip are accompanied by changes in throw and plunge of the slip vector (Faure Walker et al., 2009, 2010, 2015; Wilkinson et al., 2015; see Figures 1c and 1d). We attempt to verify this for individual coseismic ruptures using the 2016 Italian earthquakes and three other large magnitude normal faulting earthquakes that produced surface ruptures reported in the literature. We calculate the horizontal strain for fault locations outside the bend (we refer to these locations as the "outer fault segments"; see Figures 6 and 7 in Faure Walker et al., 2009, and Figures 5 and 8 herein). Equation (1), adapted from equations 13–17 from Faure Walker et al. (2010), shows how strain rate along a specified direction, φ, is calculated using field measurement of strike, dip, slip vector azimuth, and coseismic throw.

$$\dot{\varepsilon}_\varphi = \left(\frac{1}{2at}\right)\Sigma_{k=1}^{K}L^k T^k cotp^k\left[\sin\left(\phi^k - \Phi^k\right) - \sin\left(\phi^k + \Phi^k - 2\varphi\right)\right] \tag{1}$$

$\dot{\varepsilon}$ = strain rate (/year), a = area of grid square (km^2), t = time (year), L = fault length (km), T = throw (m), p = plunge (degrees), ϕ = slip vector azimuth (degrees), Φ = fault strike (degrees), and dip = fault dip angle (degrees).

To calculate the expected coseismic throw across the bend, we rearrange equation (1) to express throw as a function of strain and field measurements of strike, dip, and slip vector azimuth across the bend (equation (2)). In our calculations of throw across the bend, the inferred strain magnitude across the fault bend is assumed to be the mean of the strain calculated on the outer faults either side of the bend.

$$T = \frac{mean\ strain\ across\ outer\ faults\ per\ given\ length}{\left(\frac{1}{2a}\right)cotp^B\left\{\sin\left(\phi^B - \Phi^B\right) - \sin\left(\phi^B + \Phi^B - 2\alpha\right)\right\}}, \tag{2}$$

with ^{B} representing the value within the bend, α = principal angle of the outer fault segments measured clockwise from north (Faure Walker et al., 2010; Fung, 1977), and p (plunge) is defined as

$$p = acr\tan\left(\sin(\phi - \Phi)\tan(dip)\right). \tag{3}$$

Given the values of strain, strike, and slip vector azimuth at the bend, we iterate the fault dip in order to obtain a coseismic throw consistent with the field measurements of throw across the bend. The consistency between the iterated dip necessary to obtain a modeled throw consistent with field measurements of throw and the field measurements of dip indicates that the anomalously large throw (and hence large magnitude of the slip vector) across the bend can be explained by the relationship between horizontal strain and fault geometry.

To obtain strike values that represent the overall character of the fault bend and of the outer faults, for distances of hundreds of meters along the fault, strike lines (also known as structure contours) were constructed. Strike lines are horizontal lines joining points of equal elevation on a structure such as the hangingwall cutoff (Figure 5b; see details in Figure S4). We used our field measurements to obtain the dip (Figure 6).
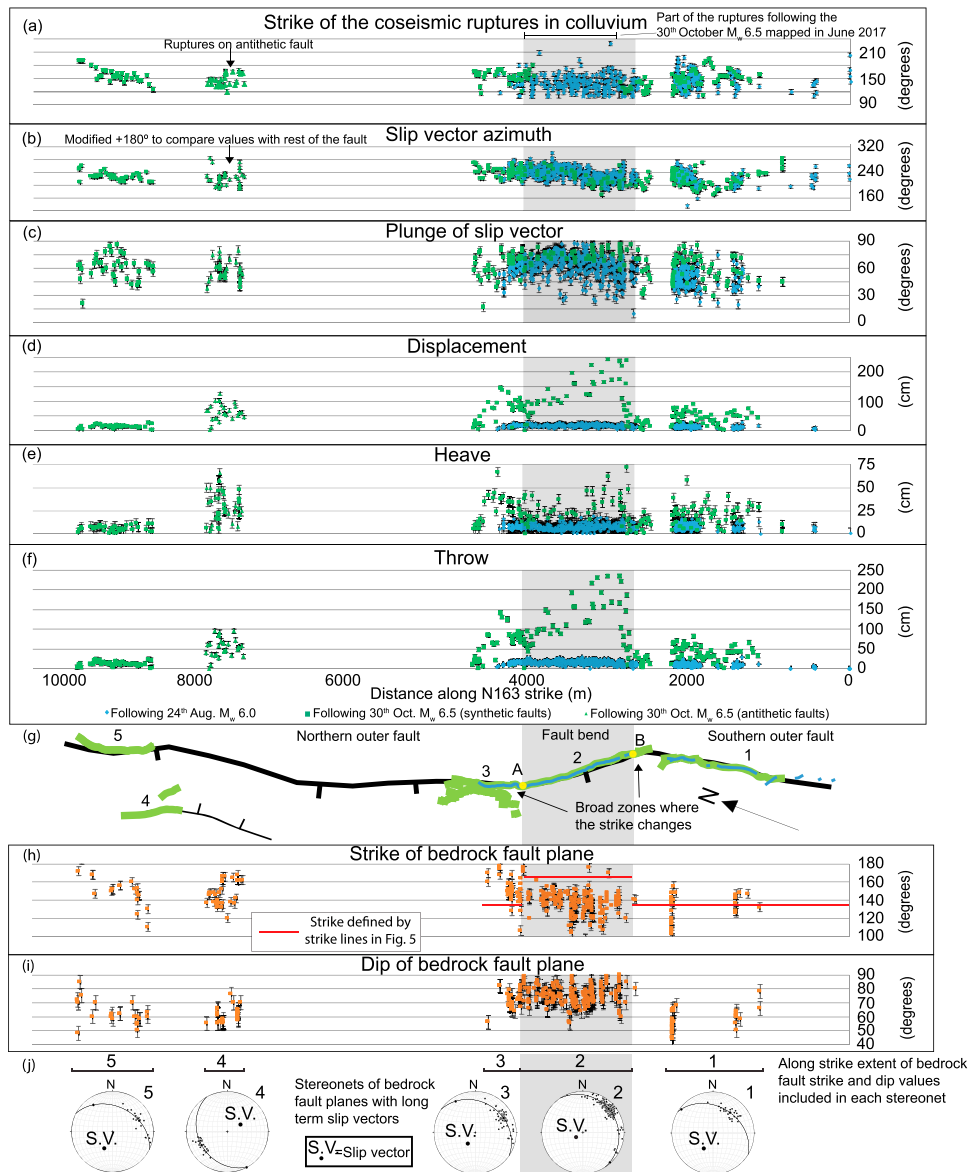
Figure 6. Field data following the 24 August and 30 October earthquakes. Panels a–f are measurements of the coseismic surface ruptures: In blue are measurements of the coseismic ruptures following the 24 August M_w 6.0 earthquake; in green are measurements of the coseismic ruptures following the 30 October M_w 6.5 earthquake. Panels h–j are measurements of the bedrock fault plane. Horizontal black bar in (a) highlights the part of the ruptures following the 30 October event mapped in June 2017. Error bars of $\pm5°$ for strike, slip vector azimuth and plunge of slip vector and of ±5 cm for displacement, heave and throw are reported as gray lines for field measurements, although errors as large as ±6 cm are plausible for throw for some of the largest values. (a) Measurements of the strike of coseismic ruptures within colluvium. The plot shows that field measurements following the two earthquakes are consistent, and both present a large local variability of strike measurements. (b) Measurements of the slip vector azimuth from both bedrock fault planes and colluvium (see details on slip vector azimuth determination in the field in the text). Measurements on the antithetic fault have been modified by $+180°$ to make them comparable with the rest of the fault. The plot shows that the azimuth of the slip vector is consistent between the two events. (c) Measurements of the plunge of the slip vector; the plot shows that the plunge increases within the fault bend for both earthquakes. Note that where it was not possible to measure it in the field, the plunge has been derived with trigonometry. (d) Measurements of the displacement across the coseismic ruptures. The displacement has been measured in the vertical plane containing the slip vector azimuth; the plot shows that displacement values increase within the fault bend. (e) Measurements of the heave of the coseismic ruptures. The plot shows that the heave is relatively consistent along the fault and does not show a clear relationship with the fault bend. Note that where it was not possible to measure heave in the field, the value was derived with trigonometry. (f) Measurements of the throw for the coseismic ruptures. The plot shows that throw values increase within the fault bend. (g) Fault map of the sector of the Mt. Vettore fault mapped in detail; in blue are the surface ruptures mapped following the 24 August M_w 6.0 earthquake; in green surface ruptures mapped following the 30 October M_w 6.5 earthquake. The bend A-B is located in Figure 5, as are the locations of the northern outer fault and southern outer fault. (h) Measurements of the strike of bedrock fault planes. These field measurements of strike show a large variability of values (see Figure S3), so red lines show strikes derived from strike-lines (see Figure 5b). (i) Measurements of the dip of the bedrock fault planes. The plot shows that the dip increases within the fault bend. (j) Stereonets of different sectors of the fault (numbers coded as in g), showing the long-term slip vectors derived from calculation of the best fit of poles to measured bedrock fault planes.

We used published structural data to study coseismic throw across along-strike fault bends for other active normal ruptures (1887, Sonora earthquake, M_w 7.5, Suter, 2008a, 2008b, 2015; 1981, Corinth earthquake, M_w 6.7–6.4, Jackson et al., 1982; Morewood & Roberts, 2001; 1983, Borah Peak earthquake, M_w 7.3, Crone et al., 1987; Figure 10a) and supplemented data for the Corinth example with our own fieldwork results. The above data were used to predict the coseismic throw in along-strike fault bends for comparison with measurements of the same, as was done for the Mt. Vettore earthquake sequence studied herein.

The reader should note that the above calculations apply only once a rupture is throughgoing and has crossed a bend. We emphasize this because there are natural examples of normal faulting ruptures that terminated at along-strike fault bends. Biasi and Wesnousky (2017) discuss the termination of some ruptures at fault bends, and it is beyond the scope of this paper to discuss this further, but we point out that all five of the earthquake ruptures we describe in this paper did cross fault bends.

4. Results

4.1. Field Observations

In the 24 August 2016 earthquake, surface ruptures formed either on the bedrock fault scarp, forming a freshly exposed stripe on the fault plane, or a few meters into the hangingwall, for a length of about 5 km along strike, propagating across a prominent along-strike fault bend (Figures 3, 4, 5 and S2). Surface ruptures were identified on the Mt. Vettore fault with a footwall made of competent limestone, whereas there are few clear signs of surface ruptures on the Laga fault, which has a footwall made mainly by less competent flysch (Livio et al., 2016). On the Mt. Vettore fault, the ruptures were continuous for about 2 km across the fault bend. The rupture was less continuous toward the SE and NW terminations of the rupture. The surface ruptures were organized as sets of well-defined partially overlapping traces, tens of meters in length, each with a local *Dmax*. Rupture traces were arranged with both right- and left-stepping en echelon relay zones placing overlapping tip zones a few decimeters to meters apart across strike. Ruptures could be traced along strike from fault traces within colluvial deposits onto bedrock fault planes and *vice versa* (Figure 4b).

The combined effect of the 26 October 2016 M_w 5.4 and 5.9 and the 30 October 2016 M_w 6.5 earthquakes appears to have ruptured the entire Mt. Vettore fault, reactivating the surface ruptures produced by the 24 August M_w 6.0 earthquake (Figure 5). Given the location of the mainshock, the 26 October M_w 5.9 earthquake appears to have ruptured only the northern part of the fault (Figure 3). Due to the short temporal interval between the 26 October and 30 October events, we were unable to determine whether the surface ruptures of the northern part of the fault were in part caused by the 26 October Mw 5.4 and 5.9 earthquakes or if the measured surface rupture was formed entirely by the larger 30 October M_w 6.5 earthquake, so these northern parts of the rupture were not included in this study. The surface ruptures in the central and southern parts of the fault, on which we focused our field mapping, were all attributable to the 30 October M_w 6.5 earthquake, based on the magnitude of slip and their timing of formation (Civico et al., 2018; Villani, Civico, et al., 2018). The 30 October surface ruptures were significantly longer and more continuous, with more slip for each rupture trace, than ruptures associated with the 24 August earthquake. The ruptures mainly occurred on bedrock fault planes, and as synthetic ruptures in colluvial deposits adjacent to the main Mt. Vettore fault escarpment. However, in places, synthetic and antithetic ruptures occurred a few tens to a few thousand meters into the hangingwall (Figure 5). Where it ruptured on bedrock, the coseismic slip produced a second freshly exposed stripe on the fault plane (Figures 4ci, 4civ, 4cv, and 4d). Presence of a mud smear covering the fault plane (Figure 4ciii) allowed us to define portions of the fault plane exhumed by the 24 August (white stripe, no mud smear due to wind and rain since 24 August) and the 30 October earthquakes (mud smear deformed by tool tracks and frictional wear striae observed a few days after the event). By June 2017, mud smears on the fault planes were no longer preserved, but it was still possible to recognize two generations of light-colored stripe on the fault planes, belonging to the two different earthquakes (Figures 4ci and 4d).

All the parameters measured in the field show high variability along strike, even over a few tens of meters (Figure 6; see Figure S2 for details of the 24 August ruptures). This is because individual rupture traces were as short as a few meters to tens of meters, and we were able to capture changes in parameters along each individual rupture trace due to our dense sampling. Despite the small-scale variability revealed by our measurements, we point out four overall features:
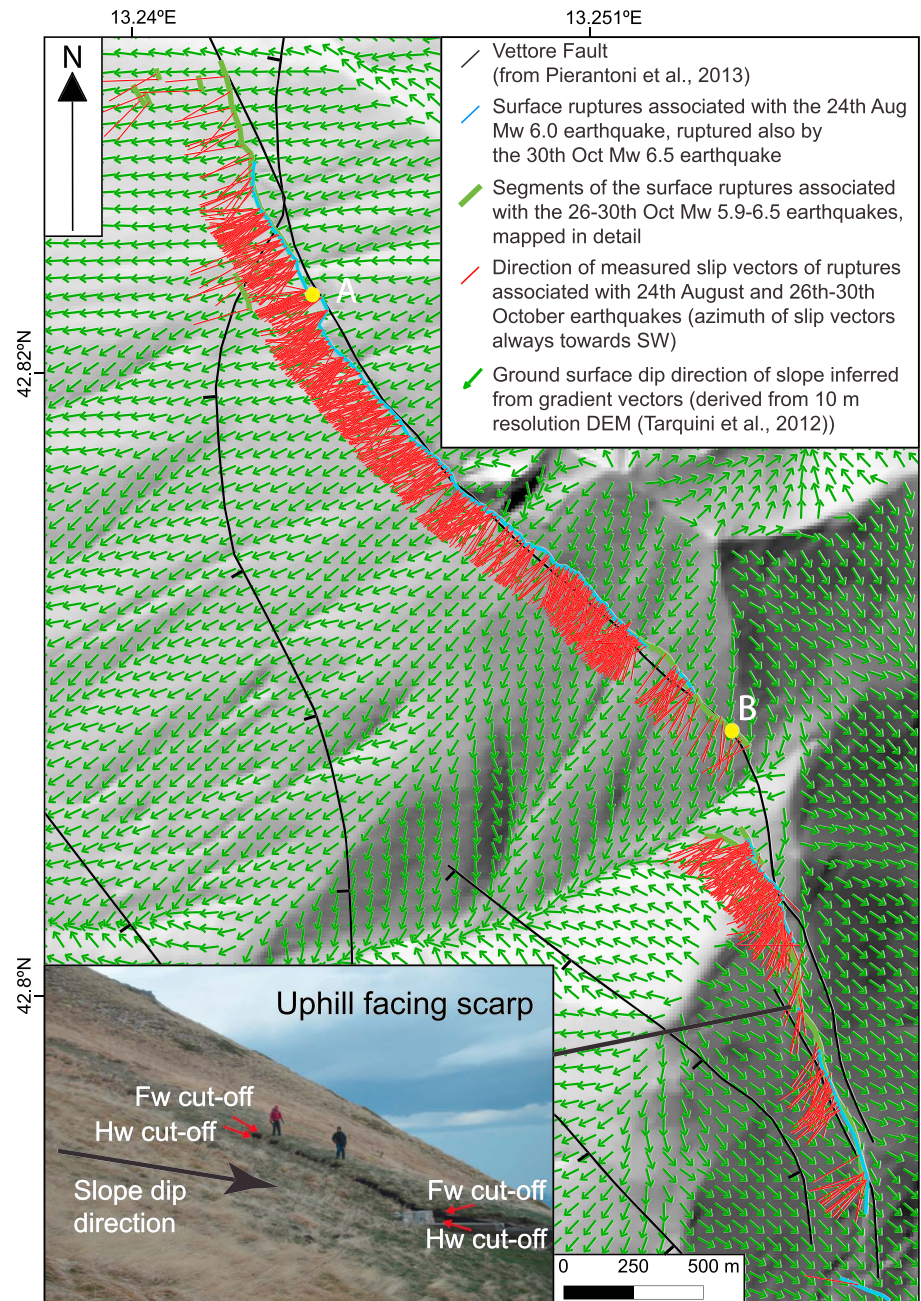
Figure 7. Comparison between the measured slip vector azimuths from both earthquakes (red lines) and the slope dip directions (green arrows). The slope dip directions are derived from a 10-m resolution DEM (Tarquini et al., 2007, 2012). Slip vector azimuths are also shown in Figure 6b. The photo in the inset shows an uphill-facing rupture with slip vectors across and/or almost opposite to the slope dip direction (two people provide scale). Our interpretation is that the direction of the measured slip vectors does not correlate with the slope dip directions; hence, this does not support the hypothesis that gravitational processes generate the surface ruptures.

1. The range of strike values for the surface ruptures is similar between the two different earthquakes. Measurements of both the coseismic ruptures in colluvium and the strike of the bedrock fault planes show a large variability of values: The strike ranges between N110° and N210° for ruptures in colluvium (Figure 6a) and between N110° and N178° for bedrock fault planes (Figure 6h). Such variation is common on bedrock fault scarps where multiple measurements are available to constrain variability (Roberts, 2007;

Figure S3). Fault plane orientations are organized so that the fault can accommodate the slip vector, so individual compass measurements of fault plane strike are not a good indicator of the overall strike of the fault (see Figure S3). Strike lines, which are a better way to gain the overall strike of the fault over along-strike distances of hundreds to thousands of meters, show that the fault strike is ~N163° to the north-west and south-east of the bend and N135° within it (Figure 5).

2. The dip of the bedrock fault plane is steeper in the fault bend, where it ranges between 70° and 88°, compared with ranges between 50° and 70° on the outer faults (Figure 6i).

3. The slip vector azimuths are very similar for both earthquakes: They range between N210° and N270°, which is consistent across the mapped fault strands (Figure 6b) and consistent with the regional stress field and 2016 focal mechanisms (Mariucci & Montone, 2016). We derived the overall azimuth of the slip vector across the fault bend and the outer faults by combining measurements of the coseismic slip vector azimuth with calculations of the best fit to poles of fault planes (see Roberts, 2007, and Figure S3 for explanation of the latter method). This shows that the slip vector azimuth is relatively constant along the fault trace (Figures 6b, 7 and S3). The overall coseismic slip vector azimuth is thought to be best represented by measurements close to the center of mapped ruptures (Roberts, 2007), and our measurements suggest a value of ~253° (see Figure S3), perpendicular to the overall fault strike, and oblique to the bend A-B again consistent with the regional NE-SW oriented extensional stress field and 2016 focal mechanisms (Mariucci & Montone, 2016). The plunge of the slip vector is also similar between the two earthquakes, with values increasing within the fault bend, where it ranges between 60° and 80°, compared to values along the outer faults, where it ranges between 40° and 70° (Figure 6c). The change in the plunge of the slip vector within the fault bend suggests that the Mt. Vettore fault is not a perfectly corrugated fault surface, in fact exhibiting a noncylindrical geometry (see Roberts, 2007, for explanation).

4. Values recording the magnitude of slip appear to increase across the bend for both surface-rupturing earthquakes (Figures 6d, 6e, 6f and S2). The throw for the 24 August earthquake is less than 12 cm along the southern outer fault and increases to a maximum of 29 cm within the bend (Figures 6f and S2). For the 30 October earthquake, throw is less than 90 cm along the southern outer fault, increases within the fault bend to a maximum of 234 cm, and decreases across the northern outer fault to less than 150 cm (Figure 6f). Similar patterns are evident for field measurements of displacement (Figures 6d and S2). Evidence for along-strike variability for heave is less clear, suggesting that the magnitude of horizontal extension was, in general, conserved across the bend, away from the tips of the overall ruptures (Figures 6e and S2). Importantly, values for offset do not appear to be affected by propagating through different materials (e.g., colluvial deposits and carbonate bedrock) with similar values where ruptures propagated from one material to the other (Figure 4bi).

To assess whether the observed scarps could be related to shallow gravitational motions (e.g., Huang et al., 2017, for the 24 August 2016 earthquake) instead of coseismic slip, we compared the azimuth of slip vectors measured across the ruptures with slope dip directions, derived from a 10-m resolution digital elevation model (Tarquini et al., 2012, Figure 7). The slip vector azimuths associated with the two earthquakes appear to be independent of the slope dip direction. In particular, the coseismic slip vector azimuth points across the slope or upslope in some locations, especially near the southern end of the rupture trace. Our interpretation is that the overall uphill-facing scarp geometry near its southern termination, and the lack of correlation between slip vector azimuths on the faults and the dip direction of the local slope, indicates a primary tectonic origin of the surface ruptures. We suggest that coseismic slip from depth propagated upwards to offset the ground surface, consistent with results measured with Global Navigation Satellite System (GNSS) located in the footwall and hangingwall of the Mt. Vettore fault, which recorded the very rapid formation of the ruptures (2–4 seconds) (Wilkinson et al., 2017).

Overall, the key observation is that the fault bend A-B was the site of anomalously large throw and displacement in both the 24 August and 30 October earthquakes; this is where the fault strike changes by about 28° and the dip steepens by about 20°.

4.2. Comparison Between Long-Term and Coseismic Activity of Mt. Vettore Fault

The long-term fault offset varies along the strike of the Mt. Vettore fault, with local maxima evident within the along-strike fault bends (Figure 8). The maximum total throw for the Mt. Vettore fault is ~1,400 m since the initiation of faulting at 2–3 Ma (Roberts & Michetti, 2004; Roberts et al., 2002), and it is located within
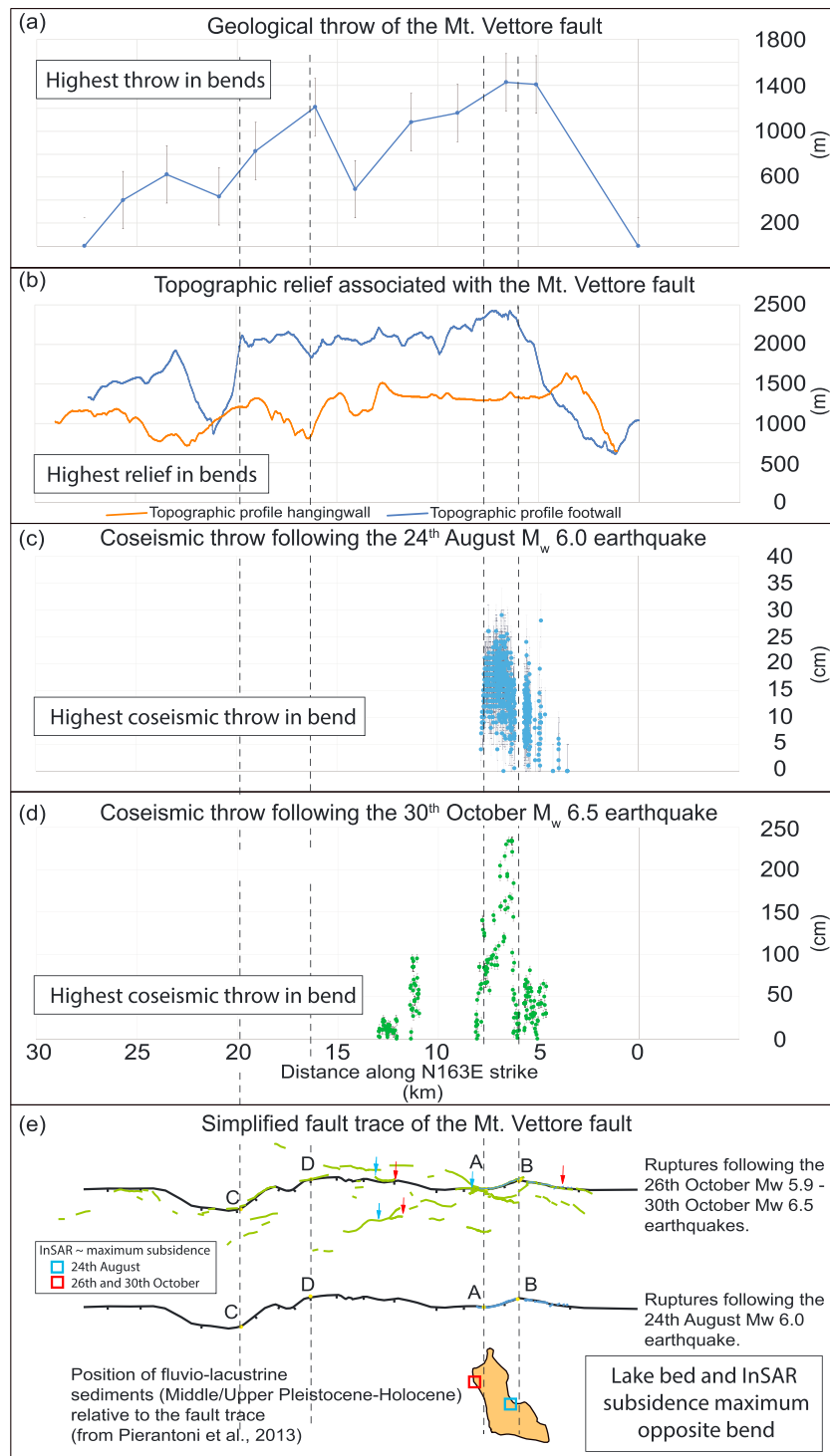
Figure 8. Comparison between (a) the geological throw profile of the Mt. Vettore fault, obtained from geological cross sections, (b) the fault-related relief of the Monti Sibillini range (footwall of the Mt. Vettore fault), (c) the coseismic throw profile for 24 August M_w 6.0 earthquake, (d) the coseismic throw profile for the 30 October M_w 6.5 earthquake, and (e) the along-strike extent of the ruptures, the lake bed location, and preliminary InSAR measurements of maximum subsidence. All the measurements are projected across strike onto a line with N163° strike, parallel to the overall strike of the Mt. Vettore fault. Error bars of ±5 cm for coseismic throw, ± 250 m for geological throw, are reported in gray. Two along-strike fault bends, marked as A-B and C-D, are shown in (e). The figure shows that the maxima in coseismic throws for the two earthquakes, the maximum in geological throw and the largest topographic relief are located adjacent to the along-strike fault bend A-B. Moreover, the lake bed and the maximum of subsidence in preliminary InSAR are located adjacent the bend A-B. Another maximum in the geological throw and in the topographic relief are also located within the along-strike fault bend C-D. Overall, the figure shows that the along-strike bends have influenced both long-term and coseismic throw along the Mt. Vettore fault.
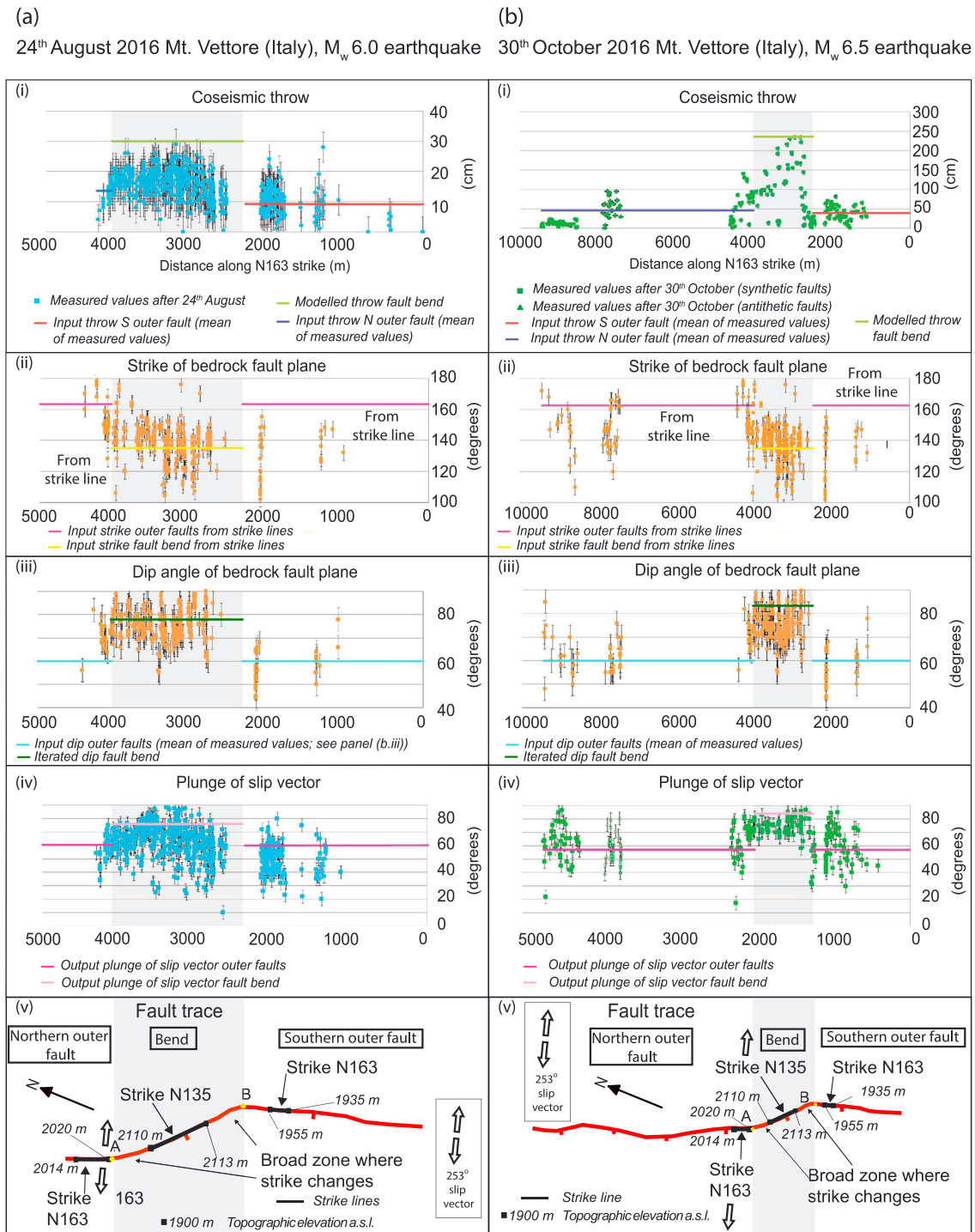
Figure 9. Modeling the (a) 24 August M$_w$ 6.0 and (b) 30 October M$_w$ 6.5 earthquakes. For each of the earthquakes, we report field measurements of coseismic throw (panels ai and bi), measurements of the strike of the bedrock fault plane (panels aii and bii), measurements of the dip of bedrock fault plane (panels aiii and biii), measurements of the plunge of the slip vector (panels aiv and biv), and the relative fault traces (panels av and bv). We have used these field measurements to model the throw and dip values across the fault bend, given the conservation of the strain and constant slip vector azimuth along the fault. In each panel colored lines represent the values that have been used in the calculation. Across the outer faults, we used the arithmetic mean of the field measurement for throw, dip, and plunge of the slip vector to calculate the strain. For strike measurements (panels aii and bii), we have used the values of strike derived from strike lines. Across the bend, iterated fault dips (reported as green lines in panels aiii and biii) are needed to obtain a coseismic throw consistent with field measurements, constant slip vector azimuth and with constant strain (green lines in panels ai and bi). In fault trace panels (av and bv), we report the subdivision of the fault in outer faults and fault bend, and the overall slip vector azimuth that we have used in the calculations (see text for details of how the slip vector azimuth is defined from field measurements). This shows that the elevated coseismic throw values can be explained by the presence of the bend and its associated steep fault dip.

the fault bend A-B (Figure 8a). A second local maximum abuts the fault bend C-D (Figure 8a). The fault-controlled relief, which developed at least partially since 2–3 Ma, reaches a maximum value of ~1,000 m within the fault bend A-B, again with a second maximum close to the bend C-D (Figure 8b). Where the hangingwall profile is higher than the footwall profile, this indicates uphill facing scarps (southeastern termination, see Figure 7 inset) or erosion of the footwall by fluvial drainage. The maximum fault-related subsidence since the Middle Pleistocene is centered opposite fault bend A-B indicated by the local presence of fluvio-lacustrine sediments in the hangingwall (Figure 8e); this is consistent with the notion that rates of vertical motion are relatively high within the fault bend since the middle Pleistocene, including the incremental offset of post last glacial maximum units within the valley (Villani & Sapia, 2017). Moreover, the maximum coseismic subsidence indicated by preliminary InSAR results for both earthquakes show maxima located near the lake bed (Figure 8e). Overall, Figure 8 suggests that the along-strike fault bend A-B, and perhaps also C-D, have been persistent features that have influenced the development of vertical motions across the Mt. Vettore fault for a time period encompassing hundreds to thousands of earthquakes.

4.3. Modeling the Expected Throw Within Fault Bends
4.3.1. Earthquakes on the Mt. Vettore Fault

We apply equations (1) and (2) using field measurements of the Mt. Vettore earthquakes. The fault strike values derived from strike lines for the Mt. Vettore fault are N163° for the outer fault segments and N135° for the bend (Figure 5b). We use a dip of 60° for the outer fault segments, which is the arithmetic mean of the measured dips. We set the slip vector azimuth to N253° on the entire fault, consistent with our field measurements (Figures 6 and S3). We set values for coseismic throws for the outer fault segments using the arithmetic means of our field measurements for each earthquake, including all the measurements obtained on the outer faults. We have used those parameters to constrain the outer faults, in order to calculate the modeled throw and dip within the bend.

For the 24 August earthquake, we used a value of 9 cm for the throw on the southern outer fault and 14 cm for the northern outer fault. We found that a fault dip in the bend of 77° produces a modeled throw of 29 cm. The iterated dip across the bend, which is necessary to model a throw value consistent with field measurements (maximum measured throw 29 ± 5 cm), is consistent with field measurements of dip across the bend (mean of measured dip $75° \pm 6°$ ($\pm 1\sigma$)).

For the 30 October earthquake, we used throws across the outer faults of 39 and 46 cm. We found that a fault dip in the bend of 84° produces a modeled throw of 233 cm, which is consistent with the maximum measured throw of 234 ± 6 cm. The 84° dip is a value consistent with our measurements of dip at locations of maximum throw, with arithmetical mean of $86° \pm 3°$ ($\pm 1\ \sigma$).

Overall, for the Mt. Vettore earthquakes our model iterations suggest throw values consistent with field measurements of throw across the bend, and field measurements of fault dips within the bend. This suggests that the conservation of the strain within an along-strike fault bend influences the coseismic throw values (Figure 9). This suggests that the 29- and 234-cm coseismic throws across the fault bend for the two earthquakes are required to preserve the extensional strain along the strike of the studied portion of the Mt. Vettore ruptures. This also further supports the interpretation that the observed offsets are due to primary tectonic faulting that propagated to the surface from seismogenic depths, rather than resulting from shallow gravitational processes (cf. Huang et al., 2017, for the 24 August 2016 earthquake).

4.3.2. Coseismic Offsets for Other Large Normal Faulting Earthquakes

To evaluate whether bends influence offsets elsewhere, we examined displacement data from surface ruptures for the 1887 M_w 7.5 Sonora earthquake (Suter, 2008a, 2008b, 2015), 1981 Corinth M_w 6.7–6.4 earthquake (Jackson et al., 1982; Morewood & Roberts, 2001; Roberts, 1996), and the 1983 M_w 7.3 Borah Peak earthquake (Crone et al., 1987; Figure 10a). In addition, we carried out new fieldwork on the 1981 Corinth ruptures in 2017 to update values from Roberts (1996). Fault traces for these earthquakes show prominent along-strike fault bends, 2–10 km long, whose presence are confirmed by the construction of strike lines (Figure 10a, panels iii, vi, and ix; see also Figure S4). Other smaller bends may exist, but we were unable to verify these because of the resolution of the field measurements of throw (average spacing of measurements for the Sonora earthquake is 528 m, for the Corinth earthquake is 1,070 m, for the Borah Peak earthquake is 426 m). We can only resolve variation in throw across bends with along-strike length longer than the average spacing of the field measurements of throw, so we concentrated on the prominent along-strike fault bends, which are also identifiable with strike lines (Figure 10a, panels iii, vi, and ix). These
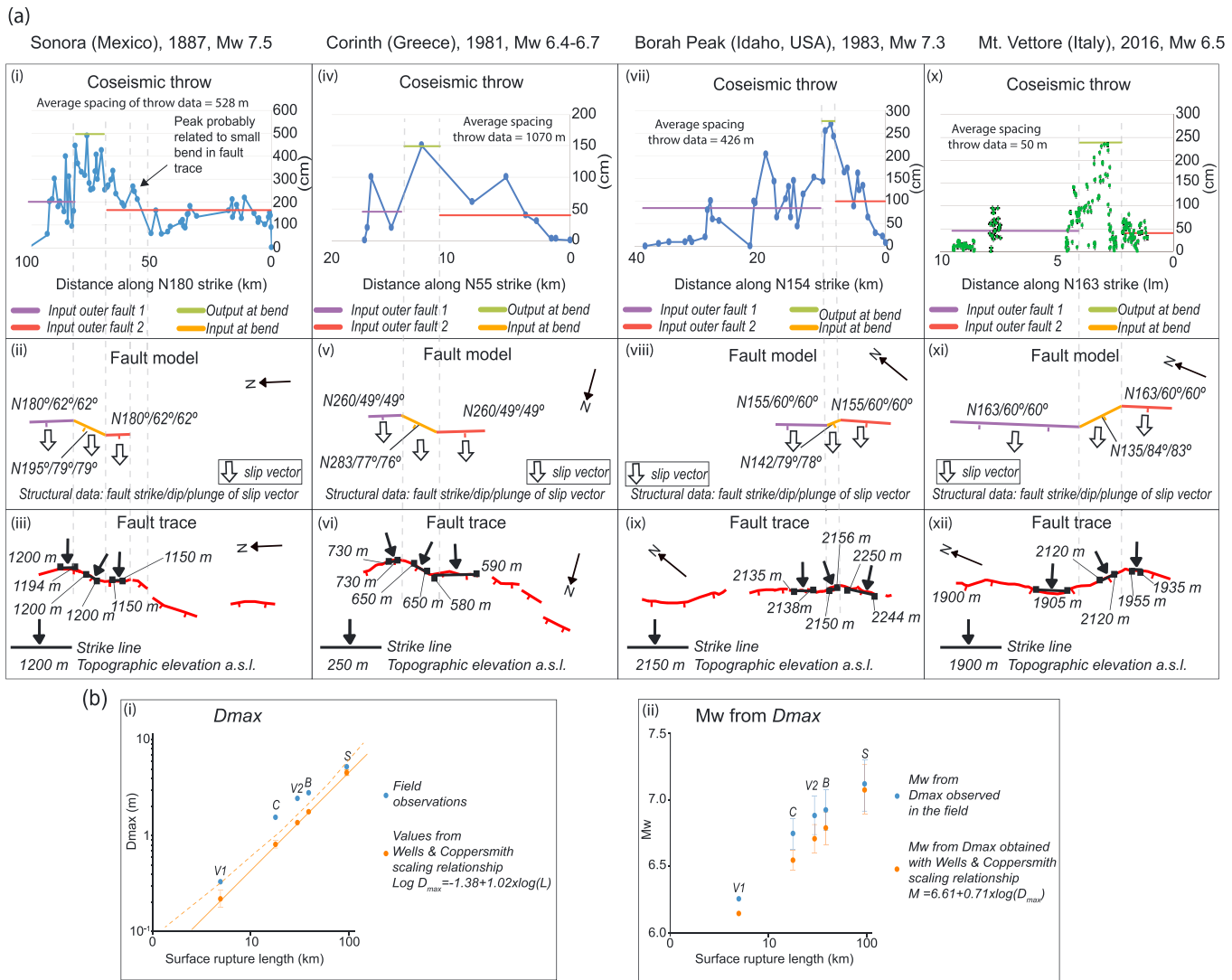
Figure 10. (a) Modeling of historical earthquakes that ruptured across along-strike fault bends. Datasets for the coseismic slip and fault trace are from Suter (2008a, 2008b, 2015), for the 1887, Sonora earthquake, M_w 7.5; Jackson et al. (1982) and Morewood and Roberts (2001), and fieldwork (see S5) for the 1981, Corinth earthquake, M_w 6.7–6.4; Crone et al. (1987), for the 1983, Borah Peak earthquake, M_w 7.3. We used the same approach shown in Figure 9. In coseismic throw panels (i, iv, vii, and x) we report along-strike throw profiles for each earthquake. For each of the panel, the average spacing of measurements reported is the average distance between the field measurements of throw for each earthquake, which represents the lower limit of spatial resolution for the identification of fault bends. In fault model panels (ii, v, viii, and xi), the input parameters of strike, dip, and plunge of the slip vector used to model the throw across the bends are indicated, as well as the slip vector azimuth used for the earthquakes. Colors are coded to input values of throws in the panels above. In fault trace panels (iii, vi, ix, and xii) we show simplified fault traces of the earthquakes, on which are reported strike lines used to define the along-strike fault bends. (b) Comparison between *Dmax* (i) and the expected M_w for *Dmax* (ii) for given fault lengths from field data obtained from the scaling relationships in Wells and Coppersmith (1994). We used our field measurements of *Dmax* for the Mt. Vettore; for the historical earthquakes, we calculate *Dmax* from maximum throws, using the value of iterated fault dip. V1 = M_w 6.0 24 August 2016 Mt. Vettore earthquakes; V2 = M_w 6.5 30 October 2016 Mt. Vettore earthquake; C = M_w 6.4–6.7 Corinth earthquake; B = M_w 7.3 Borah Peak earthquake; S = M_w 7.5 Sonora earthquake. For values derived from the Wells and Coppersmith (1994) scaling relationships, error bars, derived from standard errors reported in their Tables 2b and 2c, are reported. When the error bar is not visible, it is smaller than the symbol. In (bi), the dashed line is the upper 95% confidence interval of the *Dmax* versus fault length scaling relationship (Wells & Coppersmith, 1994). Overall, (b) shows a preponderance of higher values for the observed *Dmax* versus fault length relationship compared to those predicted from Wells & Coppersmith (1994).

bends exhibit localized maxima in coseismic throw for the surface ruptures (Figure 10a, panels i, iv, and vii) and increases of fault dip, as confirmed by published data for the Sonora earthquake (Suter, 2008a, 2008b, 2015) and from our own fieldwork for the Corinth earthquake (see Figure S5b). We have not identified detailed fault dip data for the Borah Peak earthquake, although published photos suggest that dip may be steeper within the fault bend (e.g., Figure 6 of Crone et al., 1987).

We have applied the methodology explained in section 3.2 to investigate whether the fault bends explain coseismic throw maxima. As for the Mt. Vettore earthquakes, for each earthquake we derived fault strike values from strike lines, and fault dips and throws for the outer faults as the arithmetical means of field measurements reported along the entire fault traces outside the bends, and the slip vector azimuth from field measurements. We then iterated the fault dip angles within the bends, in order to derive modeled throws across the fault bends to check for consistency with field measurements (see Figures 10a and S6 for details about input values used for each earthquake).

For the Sonora earthquake, where ruptures outside the bend show a *Dmax* of about 400 cm, the iterated fault dip value of 79° produces a modeled throw across the bend of 498 cm; these values are consistent with field measurements (arithmetic mean of dip 79°, maximum measured throw 495 cm, from Suter et al., 2008a, 2008b, 2015; see Figures S5a and S6 for details).

For the Corinth earthquake, where ruptures outside the bend show a *Dmax* of about 100 cm, the iterated dip value of 76° produces a modeled throw across the bend of 148 cm, consistent with field measurements (maximum measured dip across the bend of 77°, from our field measurements; maximum measured throw at bend 150 cm, by Jackson et al., 1982; see Figure S5b).

For the Borah Peak earthquake, where ruptures outside the bend show a *Dmax* of about 200 cm, the iterated dip value of 79° produces a modeled throw across the bend of 270 cm, consistent with the maximum field measurements of 270 cm by Crone et al. (1987). The 79° dip is similar to that shown by a field photo within the bend (see Figure 6 of Crone et al., 1987) and agrees with measurements of fault dips between 60° and 90° mentioned in Crone et al. (1987).

Thus, for the 1981 Corinth M_w 6.7–6.4 and for the 1887 Sonora M_w 7.5 earthquakes, we suggest that the required fault dip angles across the bends are consistent with field measurements. The required fault dip across the bend for the 1983 Borah Peak M_w 7.3 earthquake is a plausible value for normal faults that represent testable hypotheses given further fieldwork, but similar to that shown in field photos. Hence, it appears that along-strike fault bends may be a key control on coseismic offset. This has implications for how *Dmax* relates to rupture length and magnitude if coseismic throws from bends are converted to displacement and/or reported as *Dmax* and included in calculations to gain *Daverage*.

A note on the modeling is that the results for modeled throw replicate the measured values very well ($R^2 = 0.999$) but the results are highly sensitive to the iterated dip and less sensitive to the input strike (see Figure S7). This highlights the importance of dip measurements; future rupture mapping and paleoseismic studies should report the dip of the fault as fully as possible if the approach advocated here is to be used. Also, it is important to note that we have applied our modeling for bends with changes in strike angle of less than 28° (compare with Biasi & Wesnousky, 2017). We did not test our model for bends with greater angles, up to a case-limit of a transform fault connecting two normal faults.

4.4. Comparison Between Field Measurements and Predictions of *Dmax* From Existing Scaling Relationships

To investigate whether existing, empirically derived scaling relationships (e.g., Wells & Coppersmith, 1994) adequately predict measured displacement values for faults with along-strike bends, we compare the *Dmax* and M_w for the two Mt. Vettore earthquakes, and the Sonora, Borah Peak, and Corinth earthquakes with the same values implied by existing scaling relationships of *Dmax* versus surface rupture length (Log*Dmax* = −1.38 + 1.02xlog(L)) and M_w versus *Dmax* (M = 6.61 + 0.71xlog(*Dmax*); published in Wells and Coppersmith, 1994; Figure 10b; see also Figure S9). We have used both the *all kinematics* and *normal* scaling relationships expressed in Wells and Coppersmith (1994). We have used the all kinematics *Dmax* versus fault length scaling relationship because it covers the full range of fault lengths of our examples, including those from the literature (the range of surface rupture length in our examples is 5–100 km, the *normal kinematic* scaling relationship from Wells & Coppersmith, 1994, is valid for cases within a range of 3.8–75 km). We have used the normal kinematics M_w versus *Dmax* scaling relationship in agreement with the kinematics of the earthquakes on the Mt. Vettore fault and of the historical earthquakes. For the two Mt. Vettore earthquakes we have used the *Dmax* derived from our own field measurements; for the other historical earthquakes studied we have calculated the *Dmax* from measured throws at bends, on a fault plane with value of dip given by the iterated dip at bends obtained from our modeling.

The measured $Dmax$ values shown in Figure 10bi for the five studied earthquakes with fault bends are consistently higher than the $Dmax$ predicted from their lengths using the Wells and Coppersmith (1994) $Dmax$ versus surface rupture length scaling relationship. The M_w predicted from the observed $Dmax$ for the five studied earthquakes are perhaps larger than the M_w predicted based on the $Dmax$ predicted from the surface rupture length, although error bars overlap for some examples (Figure 10bii). Although we are aware that slip for the earthquakes in the Wells and Coppersmith (1994) database may well be influenced by a variety of parameters (e.g., depth of moment centroid, fault strength, and seismogenic thickness), our interpretation is that fault bends may form an important part of the explanation for the ~1 order of magnitude scatter in $Dmax$ for a given fault length (Figure 1; Wells & Coppersmith, 1994).

To explore whether fault bends can produce the high values and scatter seen in $Dmax$ versus surface rupture length scaling, we used equations (1) and (2) to calculate the expected throw across a bend for a variety of fault lengths and increasing fault dips within the bend, in agreement with field observations of steeper fault dips at bends, as shown by our five examples from the two Mt. Vettore earthquakes, and the Sonora, Corinth, and Borah Peak earthquakes. We followed the methodology outlined in section 3.2. For each fault rupture length, we calculated the strain across the outer faults with an assigned 40° fault dip (see Figure S8), pure dip slip kinematics, and a value of coseismic throw calculated using the $Dmax$ versus surface rupture length scaling relationship in Wells and Coppersmith (1994), $LogDmax = -1.38 + 1.02Log(L)$. Again, we have used the all kinematics scaling relationship because it covers the total range of rupture length explored. Across the bend, we maintain constant strain and slip vector azimuth and calculate the predicted throw by varying the fault dip in the bend in 5° increments from 40° to 85° (Figure 11a; see Figure S8). The range of dips explored (40°–85°) represents the range of dips that have been documented in databases containing many thousands of measurements from normal faults (e.g., Roberts, 2007). From each of the modeled throws we have calculated the expected $Dmax$ on a fault plane dipping with the value used in the calculation, and we have compared those with the $Dmax$ versus surface rupture length scaling relationship from Wells and Coppersmith (1994). We have also calculated the above for the scaling relationship in Wesnousky (2008); see Figure S9.

The results show that changing the fault dip can produce dramatic variability in the coseismic $Dmax$ within the fault bend (Figures 11a and S9a). The value of $Dmax$ can increase by ~1 order of magnitude for a fault bend with dip angle of 85° compared to one with a dip of 40°. A comparison between these results and measurements for normal faulting earthquakes in Wells and Coppersmith (1994) shows a similar range in $Dmax$ for a given fault length (~1 order of magnitude; Figure 11b). This suggests that the effect of fault bends is a likely contributor to the scatter in coseismic throw for a given fault length recorded in natural data sets.

5. Discussion

The along-strike throw profiles of five different coseismic surface ruptures associated with normal faulting earthquakes show that the coseismic throw, and therefore the coseismic $Dmax$, increases where ruptures propagate across along-strike fault bends characterized by steep fault dips. Quantitative relationships can explain these larger throws in terms of conservation of strain across the fault bend, where the fault dip becomes steeper.

Note that in our examples ruptures propagate across bends and do not terminate at these structural changes, as is the case for examples in the literature (e.g., Biasi & Wesnousky, 2017). Biasi and Wesnousky (2017) suggest that stiffening of mechanical resistance for dip slip ruptures occurs for bends with change in strike angle of about 50°. We hypothesize that our model is applicable for ruptures that do propagate across fault bends up to a change in strike of about 45°, corresponding to the limiting point at which the bend would be classified as a normal fault, rather than an oblique-slip or strike-slip fault. However, we note we have only tested our model herein for examples where propagation of ruptures across fault bends occurs and where the change in strike angle is up to 28°.

In terms of the relevance of our results to databases that have compiled $Dmax$ and rupture length (e.g., Leonard, 2010; Manighetti et al., 2007; Wells & Coppersmith, 1994; Wesnousky, 2008), it is unfortunately uncommon for the data sources that support these compilations to report whether data were collected from fault bends with strikes oblique to the extension direction or portions of faults striking perpendicular to the
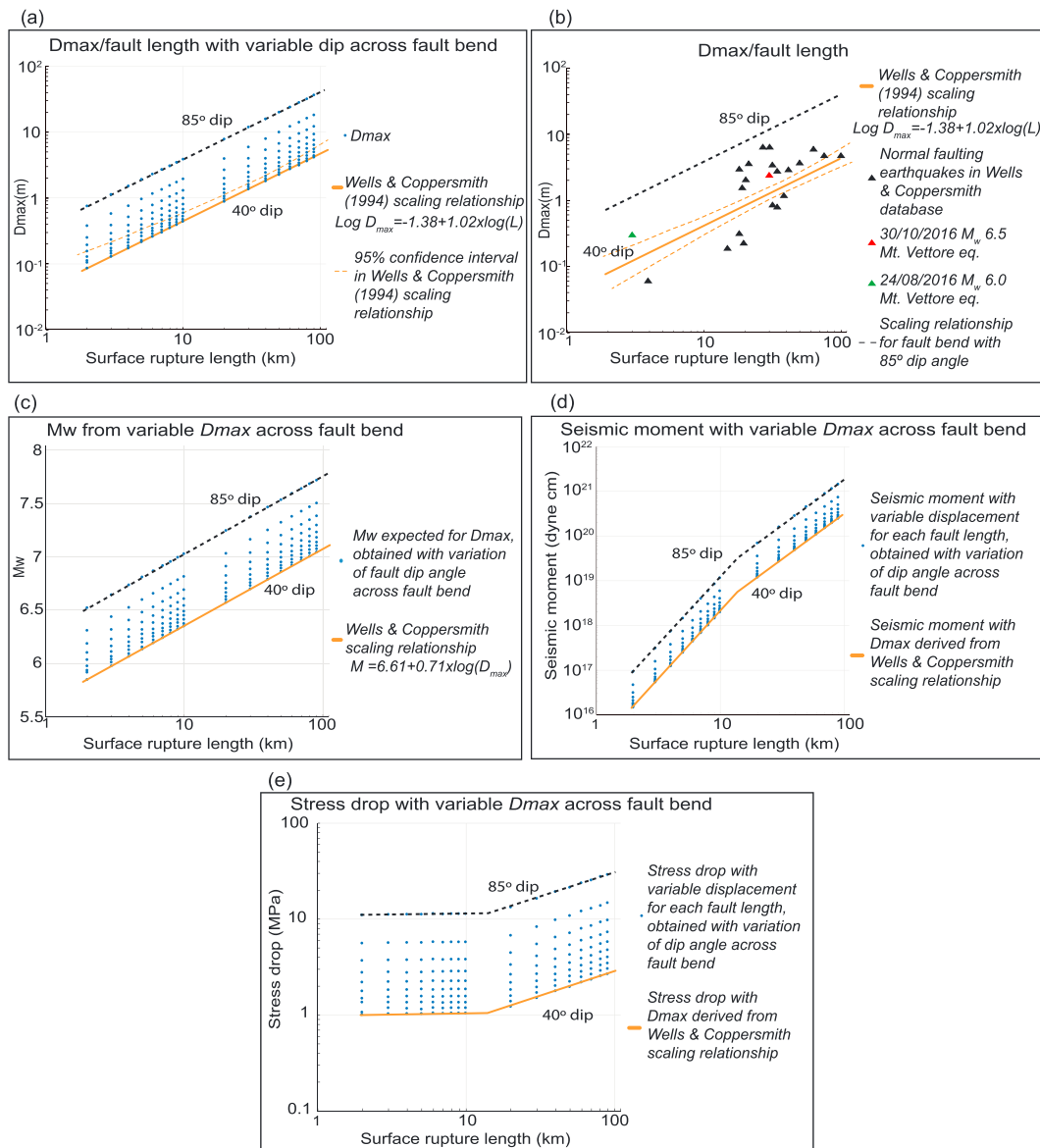
Figure 11. (a) *Dmax* versus surface rupture length scaling relationships obtained by varying the fault dip angle from 40° to 85° across an along-strike fault bend. Each *Dmax* value has been calculated from modeled throws across an along-strike fault bend, derived using equation (2). To model throws across bends, we set values for throw on the outer faults as the *Dmax* value calculated with the Wells and Coppersmith (1994) *Dmax* versus surface rupture length scaling relationship for each fault length, and a fault dip of 40°. We calculated the throw at the bend by varying values of fault dip every 5° between 40° and 85° (see Figure S8 for details). The continuous orange line represents the Wells and Coppersmith (1994), relationship. Dashed orange line is the upper 95% confidence interval of the Wells and Coppersmith (1994) relationship. Dashed black line represent values of throw for a bend with 85° fault dip angle. See Figure S9 for a similar figure for scaling relationships in Wesnousky (2008). (b) Superposition of the normal faulting earthquakes reported in Wells and Coppersmith (1994), *Dmax* versus surface rupture length graph, and related scaling relationship (continuous orange line) and 95% confidence interval (dashed orange lines), with plots of expected *Dmax* with variable dip angle across along-strike fault bend at 85°. (c) M_w derived from each *Dmax* calculated in Figure 11a. For each fault length, we have calculated the expected M_w from the modeled values of *Dmax* showed in Figure 11a using the M_w versus *Dmax* scaling relationship from Wells and Coppersmith (1994). Results are plotted with fault length on the *x*-axis to show that for each fault length, the variability of *Dmax* given by the fault bend causes a large variability in the expected M_w, when it is derived with Wells and Coppersmith (1994) M_w versus *Dmax* scaling relationship. The orange line is the regression for Mw calculated from *Dmax* obtained with the Wells and Coppersmith (1994) *Dmax* versus surface rupture length regression. (d) Seismic moment expected for each *Dmax* calculated in Figure 11a. For each fault length, we have calculated the seismic moment using the values of *Dmax* across a fault bend calculated in Figure 11a. We set the thickness of the seismogenic layer at 15 km; for fault length < 15 km we assumed a circular fault geometry. It is shown that for given fault lengths, variable displacement across fault bends can produce ~1 order of magnitude of variability in seismic moment estimations. The orange line shows the regression of seismic moment values calculated from *Dmax* obtained with Wells and Coppersmith (1994) *Dmax* versus surface rupture length scaling relationship. (e) Stress drop expected for each *Dmax* calculated in Figure 11a. The stress drops are obtained using the M_0 calculated in Figure 11d. The graph shows that variable displacement across a fault bend can induce a variability of ~ 1 order of magnitude for the stress drop value, for given fault lengths. The orange line is the regression of stress drop calculated from *Dmax* obtained with Wells and Coppersmith (1994) *Dmax* versus surface rupture length scaling relationship.

extension direction, and, in general, they do not report the geometry and kinematics of the faulting for each measurement. The observed scatter in *Dmax* for a given fault length (Figure 1) has been interpreted as indicating significant scatter in implied stress drop (Manighetti et al., 2007). Values of *Dmax* are also used in some examples to infer paleoearthquake magnitudes from paleoseismic studies, (e.g., Cinti et al., 2011; Dolan et al., 1997; Galadini & Galli, 2000, 2003; Galli et al., 2017; Galli & Peronace, 2014; Pantosti et al., 1996; Villamor & Berryman, 2001). Although careful consideration of paleoseismic uncertainties are often completed when completing state-of-the-science level hazards (e.g., Working Group on Utah Earthquake Probabilities [WGUEP], 2016), it is not a ubiquitous practice for individual investigators to consider if measurements are impacted by the effect of along-strike fault bends. We have shown that local variations in fault geometry and kinematics can produce variations in coseismic throw values, and therefore in the coseismic displacement associated with the earthquake. This leads to uncertainty in paleoearthquake magnitudes and implied variations of stress drops for a given fault length if the effect of fault bends is not considered when collecting data along prehistoric or modern fault ruptures.

We concede that it might be possible that high slip patches occur at depth, possibly propagating to the surface without the influence of fault bends, although this is difficult to prove with direct measurements at depth. Our analysis of five surface-rupturing normal fault earthquakes shows that fault bends are a plausible explanation for patches of high slip measured at the surface and that the detailed characterization of fault bend geometry allows prediction of the magnitude of the slip anomaly. Fault bends are also likely to exist at depth, and these may even be responsible for suggested high slip patches at depth. This suggests that (1) nonplanar fault geometry may be an alternative explanation of high spatial variability within slip distributions for finite fault inversions of major normal faulting earthquakes and (2) finite fault inversions should include variable fault geometry at depth, to derive the best representation of the slip distribution along the fault.

We also address how variable coseismic throws across fault bends impact calculations of M_w from *Dmax*. If the reported *Dmax* value comes from a fault bend with a high dip value, and this is not recognized, by how much might the M_w be overestimated compared to a straight fault? To answer this question, for each fault length we have calculated the expected M_w for all the plausible *Dmax* for values within the fault bend (shown in Figure 11a), using the M_w versus *Dmax* scaling relationship in Wells and Coppersmith (1994), $M = 6.61 + 0.71 \, log \, (Dmax)$, (Figure 11c). The graph shows that for a given fault length, the variability of *Dmax* across fault bends leads to a large variability of M_w estimates if M_w is derived using the M_w versus *Dmax* scaling relationship in Wells and Coppersmith (1994). This is important because fault bends, and their associated fault dip angles, are not commonly considered when using displacements measured in paleoseismic trenches to infer M_w for paleoearthquakes. It appears that this can introduce a large uncertainty of M_w into paleoseismic estimates of past seismicity.

The effect of the variability of *Dmax* on the estimation of the M_w also raises the question of how the variability in *Dmax* due to fault bends affects calculations of seismic moment and stress drop associated with normal faulting earthquakes. It is known that seismic moment and stress drop should be calculated using the *Daverage* (Kanamori & Anderson, 1975; Scholz, 2002). We also know that *Dmax ~ 2*Daverage* for most large earthquakes (e.g., Manighetti et al., 2005) and the presence of fault bends on normal faults contributes to *Dmax* being larger than *Daverage*. Therefore, we suggest that the presence of fault bends may produce bias in calculation of *Daverage* for two reasons. First, given limitations in the field due to accessibility and quality of exposure, it is possible that measurements may be focused in locations where the ruptures are more impressive and have larger offsets, which may be located within fault bends. Thus, the derived *Daverage* may contain sampling bias and overestimate the true *Daverage* if bends with high dip angles are included, but not recognized. Second, as fault bends with high dip angles produce higher values of throw, the calculated *Daverage* for a data set where measurements have been made at regularly spaced intervals along strike will contain values influenced by the high dip angles in the fault bend. Therefore, a fault with an along-strike bend with high dip angle, sampled at regular distances along strike, would have higher *Daverage* compared to that for a straight fault. Thus, claimed *Daverage* values could be biased and affect calculation of seismic moment and stress drop if the effect of bends and high dip angles are not recognized. To investigate this, we examine the worst case where *Daverage* equals *Dmax*, a scenario that could be approached if fault bends have not been considered at all, and a relatively large portion of the rupture occurs within a bend like the 24 August Mt. Vettore example.

To calculate the scalar seismic moment, we used the equation $M_0 = \mu A D$, where μ is the shear modulus (considered herein as 3×10^{10} Pa), A is the seismogenic area, and D is the *Dmax* across fault bend, derived from values in Figure 11a (Figure 11d). We set the thickness of the seismogenic layer to be 15 km. We assumed a circular fault when the fault length (L) is <15 km, and rectangular faults with increasing aspect ratio for faults with L values progressively larger than 15 km. The fault width (downdip dimension in the plane of the fault) has been corrected for different dip angles. For each fault length, the seismic moment is calculated for each displacement associated with variable fault dip. Variable displacement across fault bends can produce almost 1 order of magnitude of variability in the seismic moment estimations (Figures 11d and S9c).

To calculate stress drops, we used the equation $\Delta \sigma = c \frac{M_0}{A^{3/2}}$ (Kanamori & Anderson, 1975; Scholz, 2002; Figures 11e and S9), where C is a nondimensional shape factor (≈ 1 from Kanamori & Anderson, 1975). We used the M_0 values shown in Figures 11d and S9c to evaluate the effect of variable *Dmax* across fault bends. The results show that the variable displacement across a fault bend can produce ~1 order of magnitude of variability in stress drop values for each fault length (Figures 11e and S9d). Although this effect may be overestimated, because we are considering the worst case where *Dmax* equals *Daverage*, this result is important because information on the geometry and kinematics of faulting are not commonly considered when using D values to calculate stress drop.

Overall, we suggest that along-strike fault bends, where the fault strike becomes oblique to the slip vector azimuth and the fault dip steepens beyond what is required to maintain the slip vector, strongly influence values of coseismic throw and displacement within the bend, and thus *Dmax*. This influences the estimation of M_w from paleoseismic studies and stress drop from field data on surface ruptures. Furthermore, our findings suggest that *Dmax* to length scaling data sets are even more valuable than previously envisaged because it appears that the scatter of *Dmax* for a given length provides information about how earthquake strain and moment release are partitioned along the strike of nonplanar faults.

6. Conclusions

The 24 August 2016 M_w 6.0 and 30 October 2016 M_w 6.5 earthquakes ruptured the Laga and Mt. Vettore faults, in the central Apennines, Italy, producing anomalously large coseismic surface ruptures within an along-strike fault bend with steep fault dips on the Mt. Vettore fault. The bend has an amplitude of 0.83 km, which changes the fault strike and dip by ~25°. We characterize the surface ruptures across the bend through detailed field mapping. The fault bend and its steep dip appear to have produced (1) a local maximum in total finite slip across the fault from offset of pre-rift strata, (2) a local maximum in fault-related relief, and (3) internal drainage on the hangingwall, all three of which developed over several million years, testifying to the long-term influence of the fault bend on the coseismic throw during earthquakes.

The application of the quantitative relationships (Faure Walker et al., 2009, 2010, 2015) on field data related to these two earthquakes shows that the relatively large coseismic throw observed across the bend (29 and 234 cm for the 24 August M_w 6.0 and 30 October M_w 6.5 earthquakes, respectively) are required by the geometry and kinematics of the faulting to maintain the horizontal extensional strain along strike and across the fault bend with its high fault dip (Figure 9).

Increases of coseismic throw in fault bends are also investigated for some of the largest historic normal faulting earthquakes (1887, Sonora earthquake, M_w 7.5; 1981, Corinth earthquake, M_w 6.7–6.4; and 1983, Borah Peak earthquake, M_w 7.3). The same equations can explain the anomalously large coseismic *Dmax* values in terms of conservation of the horizontal extensional strain along-strike and across the fault bends with their high fault dips. Thus, this paper provides the first multiple examples from different normal faulting regions showing that coseismic throw depends on fault geometry. Furthermore, it is possible to quantify and explain changes in observed coseismic throws across fault bends in addition to longer-term changes in throw rates across fault bends.

We suggest that along-strike fault bends are a plausible explanation of the scatter of *Dmax* values for normal faulting earthquakes in *Dmax* versus surface rupture length scaling relationships (e.g., Wells & Coppersmith, 1994). Thus, if the role of bends and high dips in those bends are not considered, this can produce misleading interpretations of (1) M_w from *Dmax* values gathered during paleoseismological studies, (2) seismic moments, and (3) stress drops influenced by *Dmax*. This study should prompt further investigation into

the role of fault bends and their dips in influencing the magnitude of coseismic displacements associated with surface ruptures because it appears that the scatter of *Dmax* for a given length provides information about how earthquake strain and moment release are partitioned along the strike of nonplanar faults.

References

Anderson, H., & Jackson, J. (1987). Active tectonics of the Adriatic region. *Geophysical Journal International*, *91*(3), 937–983. https://doi.org/10.1111/j.1365-246X.1987.tb01675

Biasi, G. P., & Wesnousky, S. G. (2017). Bends and ends of surface ruptures. *Bulletin of the Seismological Society of America*, *107*(6), 2543–2560. https://doi.org/10.1785/0120160292

Blumetti, A. M., Dramis, F., & Michetti, A. M. (1993). Fault-generated mountain fronts in the central apennines (Central Italy): Geomorphological features and seismotectonic implications. *Earth Surface Processes and Landforms*, *18*(3), 203–223. https://doi.org/10.1002/esp.3290180304

Boncio, P., Lavecchia, G., & Pace, B. (2004). Defining a model of 3D seismogenic sources for seismic hazard assessment applications: The case of central Apennines (Italy). *Journal of Seismology*, *8*(3), 407–425. https://doi.org/10.1023/B:JOSE.0000038449.78801.05

Calderoni, G., Rovelli, A., & Di Giovambattista, R. (2017). Rupture directivity of the strongest 2016–2017 central Italy earthquakes. *Journal of Geophysical Research: Solid Earth*, *122*, 9118–9131. https://doi.org/10.1002/2017JB014118

Cavinato, G. P., & Celles, P. D. (1999). Extensional basins in the tectonically bimodal central Apennines fold-thrust belt, Italy: response to corner flow above a subducting slab in retrograde motion. *Geology*, *27*(10), 955–958.

Cavinato, G. P., Carusi, C., Dall'Asta, M., Miccadei, E., & Piacentini, T. (2002). Sedimentary and tectonic evolution of Plio-Pleistocene alluvial and lacustrine deposits of Fucino Basin (Central Italy). *Sedimentary Geology*, *148*(1-2), 29–59. https://doi.org/10.1016/S0037-0738(01)00209-3

Cello, G., Mazzoli, S., Tondi, E., & Turco, E. (1997). Active tectonics in the central Apennines and possible implications for seismic hazard analysis in peninsular Italy. *Tectonophysics*, *272*(1), 43–68. https://doi.org/10.1016/S0040-1951(96)00275-2

Cheloni, D., De Novellis, V., Albano, M., Antonioli, A., Anzidei, M., Atzori, S., et al. (2017). Geodetic model of the 2016 Central Italy earthquake sequence inferred from InSAR and GPS data. *Geophysical Research Letters*, *44*, 6778–6787. https://doi.org/10.1002/2017GL073580

Chiaraluce, L., Di Stefano, R., Tinti, E., Scognamiglio, L., Michele, M., Casarotti, E., et al. (2017). The 2016 Central Italy seismic sequence: A first look at the mainshocks, aftershocks, and source models. *Seismological Research Letters*, *88*(3), 757–771. https://doi.org/10.1785/0220160221

Cinti, F. R., Pantosti, D., De Martini, P. M., Pucci, S., Civico, R., Pierdominici, S., et al. (2011). Evidence for surface faulting events along the Paganica fault prior to the 6 April 2009 L'Aquila earthquake (Central Italy). *Journal of Geophysical Research*, *116*, B07308. https://doi.org/10.1029/2010JB007988

Civico, R., Pucci, S., Villani, F., Pizzimenti, L., De Martini, P. M., Nappi, R., & Open EMERGEO Working Group (2018). Surface ruptures following the 30 October 2016 M w 6.5 Norcia earthquake, Central Italy. *Journal of Maps*, *14*(2), 151–160. https://doi.org/10.1080/17445647.2018.1441756

Crone, A. J., Machette, M. N., Bonilla, M. G., Lienkaemper, J. J., Pierce, K. L., Scott, W. E., & Bucknam, R. C. (1987). Surface faulting accompanying the Borah Peak earthquake and segmentation of the Lost River fault, Central Idaho. *Bulletin of the Seismological Society of America*, *77*(3), 739–770.

Doglioni, C. (1993). Some remarks on the origin of foredeeps. *Tectonophysics*, *228*(1–2), 1–20. https://doi.org/10.1016/0040-1951(93)90211-2

Dolan, J. F., Sieh, K., Rockwell, T. K., Guptill, P., & Miller, G. (1997). Active tectonics, paleoseismology, and seismic hazards of the Hollywood fault, northern Los Angeles basin, California. *Geological Society of America Bulletin*, *109*(12), 1595–1616. https://doi.org/10.1130/0016-7606(1997)109<1595:ATPASH>2.3.CO;2

Falcucci, E., Gori, S., Bignami, C., Pietrantonio, G., Melini, D., Moro, M., et al. (2018). The Campotosto seismic gap in between the 2009 and 2016–2017 seismic sequences of Central Italy and the role of inherited lithospheric faults in regional seismotectonic settings. *Tectonics*, *37*, 2425–2445. https://doi.org/10.1029/2017TC004844

Faure Walker J.P., G. P. Roberts, P. A. Cowie, K. McCaffrey. L. Wedmore, Z. Watson, L. C. Gregory (2015), Long-term strain rates as a tool for understanding the mechanics of continental extension and the importance of local 3D fault geometry for local throw-rates across faults. 6th Int. INQUA meeting on Paleoseismology, active tectonics and Archaeoseismology, 19-24 April 2015, Pescina, Fucino Basin, Italy, 27 150–154.

Faure Walker, J. P., Roberts, G. P., Cowie, P. A., Papanikolaou, I. D., Sammonds, P. R., Michetti, A. M., & Phillips, R. J. (2009). Horizontal strain-rates and throw-rates across breached relay zones, Central Italy: Implications for the preservation of throw deficits at points of normal fault linkage. *Journal of Structural Geology*, *31*(10), 1145–1160. https://doi.org/10.1016/j.jsg.2009.06.011

Faure Walker, J. P., Roberts, G. P., Sammonds, P. R., & Cowie, P. A. (2010). Comparison of earthquake strains over 10 2 and 10 4 year timescales: Insights into variability in the seismic cycle in the central Apennines, Italy. *Journal of Geophysical Research*, *115*, B10418. https://doi.org/10.1029/2009JB006462

Ferrario, M. F., & Livio, F. (2018). Characterizing the distributed faulting during the 30 October 2016, Central Italy earthquake: A reference for fault displacement hazard assessment. *Tectonics*, *37*, 1256–1273. https://doi.org/10.1029/2017TC004935

Fung, Y. C. (1977). *A first course in continuum mechanics*. Englewood Cliffs, New Jersey: Prentice-Hall, Inc.

Galadini, F., & Galli, P. (2000). Active tectonics in the central Apennines (Italy)– Input data for seismic hazard assessment. *Natural Hazards*, *22*(3), 225–268. https://doi.org/10.1023/A:1008149531980

Galadini, F., & Galli, P. (2003). Paleoseismology of silent faults in the central Apennines (Italy): The Mt. Vettore and Laga Mts. Faults. *Annals of Geophysics*, *46*, 815–836.

Galli, P., Giaccio, B., Messina, P., Peronace, E., Amato, V., Naso, G., et al. (2017). Middle to Late Pleistocene activity of the northern Matese fault system (southern Apennines, Italy). *Tectonophysics*, *699*, 61–81. https://doi.org/10.1016/j.tecto.2017.01.007

Galli, P., & Peronace, E. (2014). New paleoseismic data from the Irpinia Fault. A different seismogenic perspective for southern Apennines (Italy). *Earth-Science Reviews*, *175-201*.

Huang, M. H., Fielding, E. J., Liang, C., Milillo, P., Bekaert, D., Dreger, D., & Salzer, J. (2017). Coseismic deformation and triggered landslides of the 2016 Mw 6.2 Amatrice earthquake in Italy. *Geophysical Research Letters*, *44*, 1266–1274. https://doi.org/10.1002/2016GL071687

Jackson, J. A., Gagnepain, J., Houseman, G., King, G. C. P., Papadimitriou, P., Soufleris, C., & Virieux, J. (1982). Seismicity, normal faulting, and the geomorphological development of the Gulf of Corinth (Greece): The Corinth earthquakes of February and March 1981. *Earth and Planetary Science Letters*, *57*(2), 377–397. https://doi.org/10.1016/0012-821X(82)90158-3

Kanamori, H., & Anderson, D. L. (1975). Theoretical basis of some empirical relations in seismology. *Bulletin of the Seismological Society of America*, *65*(5), 1073–1095.

Lavecchia, G., Castaldo, R., de Nardis, R., De Novellis, V., Ferrarini, F., Pepe, S., et al. (2016). Ground deformation and source geometry of the 24 August 2016 Amatrice earthquake (Central Italy) investigated through analytical and numerical modeling of DInSAR measurements and structural-geological data. *Geophysical Research Letters*, *43*, 12,389–12,398. https://doi.org/10.1002/2016GL071723

Leonard, M. (2010). Earthquake fault scaling: Self-consistent relating of rupture length, width, average displacement, and moment release. *Bulletin of the Seismological Society of America*, *100*(5A), 1971–1988. https://doi.org/10.1785/0120090189

Livio, F., Michetti, A. M., Vittori, E., Gregory, L., Wedmore, L., Piccardi, L., et al., & Central Italy Earthquake Working (2016). Surface faulting during the August 24, 2016, Central Italy earthquake (Mw 6.0): Preliminary results. *Annals of Geophysics*, *59*(5), 1–8.

Manighetti, I., Campillo, M., Bouley, S., & Cotton, F. (2007). Earthquake scaling, fault segmentation, and structural maturity. *Earth and Planetary Science Letters*, *253*(3-4), 429–438. https://doi.org/10.1016/j.epsl.2006.11.004

Manighetti, I., Campillo, M., Sammis, C., Mai, P. M., & King, G. (2005). Evidence for self-similar, triangular slip distributions on earthquakes: Implications for earthquake and fault mechanics. *Journal of Geophysical Research*, *110*, B05302. https://doi.org/10.1029/2004JB003174

Mansfield, C., & Cartwright, J. (2001). Fault growth by linkage: Observations and implications from analogue models. *Journal of Structural Geology*, *23*(5), 745–763. https://doi.org/10.1016/S0191-8141(00)00134-6

Mariucci, M. T., & Montone, P. (2016). Contemporary stress field in the area of the 2016 Amatrice seismic sequence (Central Italy). *Annales of Geophysics*, *59*. https://doi.org/10.4401/ag-7235

McLeod, A. E., Dawers, N. H., & Underhill, J. R. (2000). The propagation and linkage of normal faults: Insights from the Strathspey-Brent-Statfjord fault array, northern North Sea. *Basin Research*, *12*(3-4), 263–284. https://doi.org/10.1046/j.1365-2117.2000.00124.x

Mildon, Z. K., Roberts, G. P., Faure Walker, J. P., & Iezzi, F. (2017). Coulomb stress transfer and fault interaction over millennia on non-planar active normal faults: The Mw 6.5-5.0 seismic sequence of 2016-2017, central Italy. *Geophysical Journal International*, *210*(2), 1206–1218. https://doi.org/10.1093/gji/ggx213

Mildon, Z. K., Roberts, G. P., Faure Walker, J. P., Wedmore, L., & McCaffrey, K. J. W. (2016). Active normal faulting during the 1997 seismic sequence in Colfiorito, Umbria: Did slip propagate to the surface? *Journal of Structural Geology*, *91*, 102–113. https://doi.org/10.1016/j.jsg.2016.08.011

Morewood, N. C., & Roberts, G. P. (2001). Comparison of surface slip and focal mechanism slip data along normal faults: An example from the eastern Gulf of Corinth, Greece. *Journal of Structural Geology*, *23*(2-3), 473–487. https://doi.org/10.1016/S0191-8141(00)00126-7

Pantosti, D., D'Addezio, G., & Cinti, F. R. (1996). Paleoseismicity of the Ovindoli-Pezza fault, central Apennines, Italy: A history including a large, previously unrecorded earthquake in the Middle Ages (860–1300 AD). *Journal of Geophysical Research*, *101*(B3), 5937–5959. https://doi.org/10.1029/95JB03213

Patacca, E., Sartori, R., & Scandone, P. (1990). Tyrrhenian basin and Apenninic arcs: Kinematic relations since late Tortonian times. *Memorie della Societa Geologica Italiana*, *45*(1), 425–451.

Pavlides, S., Chatzipetros, A., Papathanasiou, G., Georgiadis, G., Sboras, S., & Valkaniotis, S. (2017). Ground deformation and fault modeling of the 2016 sequence (24 Aug. – 30 Oct.) in central Apennines (Central Italy). *Bulletin of the Geological Society of Greece*, *51*, 76–112.

Perouse, E., Benedetti, L., Fleury, J., Rizza, M., Puliti, I., Billant, J., et al. (2018). Coseismic slip vectors of 24 August and 30 October 2016 earthquakes in Central Italy: Oblique slip and regional kinematic implications. *Tectonics*, *37*. https://doi.org/10.1029/2018TC005083

Pierantoni, P., Deiana, G., & Galdenzi, S. (2013). Stratigraphic and structural features of the Sibillini Mountains (Umbria-Marche Apennines, Italy). *Italian Journal of Geosciences*, *132*(3), 497–520. https://doi.org/10.3301/IJG.2013.08

Pizzi, A., Di Domenica, A., Gallovič, F., Luzi, L., & Puglia, R. (2017). Fault segmentation as constraint to the occurrence of the main shocks of the 2016 Central Italy seismic sequence. *Tectonics*, *36*, 2370–2387. https://doi.org/10.1002/2017TC004652

Pizzi, A., & Galadini, F. (2009). Pre-existing cross-structures and active fault segmentation in the northern-central Apennines (Italy). *Tectonophysics*, *476*(1-2), 304–319.

Pizzi, A., & Scisciani, V. (2000). Methods for determining the Pleistocene–Holocene component of displacement on active faults reactivating pre-Quaternary structures: examples from the central Apennines (Italy). *Journal of Geodynamics*, *29*(3-5), 445–457.

Porreca, M., Minelli, G., Ercoli, M., Brobia, A., Mancinelli, P., Cruciani, F., et al. (2018). Seismic reflection profiles and subsurface geology of the area interested by the 2016–2017 earthquake sequence (Central Italy). *Tectonics*, *37*, 1116–1137. https://doi.org/10.1002/2017TC004915

Roberts, G. P. (1996). Noncharacteristic normal faulting surface ruptures from the Gulf of Corinth, Greece. *Journal of Geophysical Research*, *101*(B11), 25,255–25,267. https://doi.org/10.1029/96JB02119

Roberts, G. P. (2007). Fault orientation variations along the strike of active normal fault systems in Italy and Greece: Implications for predicting the orientations of subseismic-resolution faults in hydrocarbon reservoirs. *AAPG Bulletin*, *91*(1), 1–20. https://doi.org/10.1306/08300605146

Roberts, G. P., & Michetti, A. M. (2004). Spatial and temporal variations in growth rates along active normal fault systems: An example from the Lazio-Abruzzo Apennines, Central Italy. *Journal of Structural Geology*, *26*(2), 339–376. https://doi.org/10.1016/S0191-8141(03)00103-2

Roberts, G. P., Michetti, A. M., Cowie, P., Morewood, N. C., & Papanikolaou, I. (2002). Fault slip-rate variations during crustal-scale strain localisation, Central Italy. *Geophysical Research Letters*, *29*(8), 1168. https://doi.org/10.1029/2001GL013529

Rovida A., Locati M., Camassi R., Lolli B., Gasperini P. (Eds.), 2016. CPTI15, the 2015 version of the parametric catalogue of Italian earthquakes. *Istituto Nazionale di Geofisica e Vulcanologia*. doi: https://doi.org/10.6092/INGV.IT-CPTI15

Scholz, C. H. (2002). *The Mechanics of Earthquakes and Faulting*. Cambridge, UK: Cambridge University press. https://doi.org/10.1017/CBO9780511818516

Scognamiglio, L., Tinti, E., Casarotti, E., Pucci, S., Villani, F., Cocco, M., et al. (2018). Complex fault geometry and rupture dynamics of the MW 6.5, 30 October 2016, Central Italy earthquake. *Journal of Geophysical Research: Solid Earth*, *123*, 2943–2964. https://doi.org/10.1002/2018JB015603

Stirling, M., Rhoades, D., & Berryman, K. (2002). Comparison of earthquake scaling relations derived from data of the instrumental and preinstrumental era. *Bulletin of the Seismological Society of America*, *92*(2), 812–830. https://doi.org/10.1785/0120000221

Suter, M. (2008a). Structural configuration of the Otates fault (southern Basin and Range Province) and its rupture in the 3 May 1887 Mw 7.5 Sonora, Mexico, earthquake. *Bulletin of the Seismological Society of America*, *98*(6), 2879–2893. https://doi.org/10.1785/0120080129

Suter, M. (2008b). Structural configuration of the Teras Fault (southern Basin and Range Province) and its rupture in the 3 May 1887 Mw 7.5 Sonora, Mexico earthquake. *Revista Mexicana de Ciencias Geológicas*, *25*(1), 179–195.

Suter, M. (2015). Rupture of the Pitáycachi Fault in the 1887 Mw 7.5 Sonora, Mexico earthquake (southern Basin-and-Range Province): Rupture kinematics and epicenter inferred from rupture branching patterns. *Journal of Geophysical Research: Solid Earth*, *120*, 617–641. https://doi.org/10.1002/2014JB011244

Tarquini, S., Isola, I., Favalli, M., Mazzarini, F., Bisson, M., Pareschi, M. T., & Boschi, E. (2007). TINITALY/01: A new triangular irregular network of Italy. *Annals of Geophysics*, *50*, 407–425.

Tarquini, S., Vinci, S., Favalli, M., Doumaz, F., Fornaciai, A., & Nannipieri, L. (2012). Release of a 10-m-resolution DEM for the Italian territory: Comparison with global-coverage DEMs and anaglyph-mode exploration via the web. *Computers & Geosciences*, *38*(1), 168–170. https://doi.org/10.1016/j.cageo.2011.04.018

Verdecchia, A., Pace, B., Visini, F., Scotti, O., Peruzza, L., & Benedetti, L. (2018). The role of viscoelastic stress transfer in long-term earthquake cascades: Insights after the Central Italy 2016–2017 seismic sequence. *Tectonics*, *37*. https://doi.org/10.1029/2018TC005110

Villamor, P., & Berryman, K. (2001). A late Quaternary extension rate in the Taupo Volcanic Zone, New Zealand, derived from fault slip data. *New Zealand Journal of Geology and Geophysics*, *44*(2), 243–269. https://doi.org/10.1080/00288306.2001.9514937

Villani, F., Civico, R., Pucci, S., Pizzimenti, L., Nappi, R., De Martini, P. M., & the Open EMERGEO Working Group (2018). A database of the coseismic effects following the 30 October 2016 Norcia earthquake in Central Italy. *Scientific Data*, *5*, 180049. https://doi.org/10.1038/sdata.2018.49

Villani, F., Pucci, S., Civico, R., De Martini, P. M., Cinti, F. R., & Pantosti, D. (2018). Surface faulting of the 30 October 2016 Mw 6.5 central Italy earthquake: Detailed analysis of a complex coseismic rupture. *Tectonics*, *37*. https://doi.org/10.1029/2018TC005175

Villani, F., & Sapia, V. (2017). The shallow structure of a surface-rupturing fault in unconsolidated deposits from multi-scale electrical resistivity data: The 30 October 2016 Mw 6.5 central Italy earthquake case study. *Tectonophysics*, *717*, 628–644.

Walters, R. J., Gregory, L. C., Wedmore, L. N. J., Craig, T. J., McCaffrey, K., Wilkinson, M., et al. (2018). Dual control of fault intersections on stop-start rupture in the 2016 Central Italy seismic sequence. *Earth and Planetary Science Letters*, *500*, 1–14. https://doi.org/10.1016/j.epsl.2018.07.043

Wells, D. L., & Coppersmith, K. J. (1994). New empirical relationships among magnitude, rupture length, rupture width, rupture area, and surface displacement. *Bulletin of the Seismological Society of America*, *84*(4), 974–1002.

Wesnousky, S. G. (2008). Displacement and geometrical characteristics of earthquake surface ruptures: Issues and implications for seismic-hazard analysis and the process of earthquake rupture. *Bulletin of the Seismological Society of America*, *98*(4), 1609–1632. https://doi.org/10.1785/0120070111

Wilkinson, M., Roberts, G. P., McCaffrey, K., Cowie, P. A., Faure Walker, J. P., Papanikolau, I., et al. (2015). Slip distributions on active normal faults measured from LiDAR and field mapping of geomorphic offsets: An example from L'Aquila, Italy, and implications for modelling seismic moment release. *Geomorphology*, *237*, 130–141. https://doi.org/10.1016/j.geomorph.2014.04.026

Wilkinson, M. W., McCaffrey, K. J. W., Jones, R. R., Roberts, G. P., Holdsworth, R. E., Gregory, L. C., et al. (2017). Near-field fault slip of the 2016 Vettore M_w 6.6 earthquake (Central Italy) measured using low-cost GNSS. *Nature Scientific Reports*, *7*, 4612.

Working Group on Utah Earthquake Probabilities (WGUEP) (2016). Earthquake probabilities for the Wasatch Front region in Utah, Idaho, and Wyoming. Utah Geological Survey Miscellaneous Publication 16-3, 164 p., 5 appendices.